University of Alberta

Evaluation of e-beam SiO_2 for MIM application

by

Wei Guo

A thesis submitted to the Faculty of Graduate Studies and Research
in partial fulfillment of the requirements for the degree of

Master of Science
in
Materials Engineering

Department of Chemical and Materials Engineering

©Wei Guo
Spring 2010
Edmonton, Alberta

Permission is hereby granted to the University of Alberta Libraries to reproduce single copies of this thesis and to lend or sell such copies for private, scholarly or scientific research purposes only. Where the thesis is converted to, or otherwise made available in digital form, the University of Alberta will advise potential users of the thesis of these terms.

The author reserves all other publication and other rights in association with the copyright in the thesis and, except as herein before provided, neither the thesis nor any substantial portion thereof may be printed or otherwise reproduced in any material form whatsoever without the author's prior written permission.

Examining Committee

Ken Cadien, Chemical and Materials Engineering

David Mitlin, Chemical and Materials Engineering

Mani Vaidyanathan, Electrical and Computer Engineering

ABSTRACT

A metal-insulator-metal (MIM) device is used to rectify high frequency radiation received through an antenna coupled to it. In this study, a Ta-SiO_2-Ta MIM device was fabricated and characterized. SiO_2 layers with different thicknesses of 2nm, 5nm and 8nm were deposited and evaluated both electrically and optically. Tantalum was deposited using a sputtering system, while the oxide was evaporated using an E-beam evaporator. A Keithley 4200-SCS system combined with a four-probe station was adopted to measure both current-voltage and capacitance-voltage (C-V) characteristics. The I-V curves for all MIM devices were almost linear except the one with 8nm of SiO_2 exhibited some nonlinearity. The C-V measurement that was carried out at AC frequency showed changing resistance for all samples and the resistance decreased as the thickness decreased. However, the E-beam SiO_2 was found not to be a desirable oxide for MIM application due to the existence of many defects.

ACKNOWLEDGEMENTS

I would like to extend my gratitude to many people for helping in various ways to make this thesis possible. I would like to express my sincere appreciation and gratitude to my supervisor Dr. Kenneth Cadien who kindly gave me continuous support, encouragement and guidance throughout the whole project. I learned a lot from his invaluable advice and excellent ideas.

I take pleasure in thanking Les Schowalter and Scott Munro who trained me to use the tools in the NanoFab, Terry Weng who helped me with the measurement set-ups in Scanimetrics Ltd., Leslie Cadien who kindly reviewed my thesis, and my fellow colleague Harun Muhammed for his suggestions and help.

I would also like to thank the Nanofabrication Group which has created a wonderful and friendly environment throughout my years here. My gratitude also goes to the professors from Electrical Engineering who gave me advice and suggestions.

I want to thank my friends for their care and support throughout my graduate studies. Last but not least, my deep gratitude and love goes to my family for their precious love, understanding and support.

TABLE OF CONTENTS

CHAPTER 1: INTRODUCTION 1

1.1 Background 1

1.2 Objective of research 1

1.2.1 Selection of materials 1

1.2.2 Fabrication of MIM structure 2

1.2.3 Characterization of MIM and evaluation of insulating oxide 2

1.3 Organization of thesis 2

CHAPTER 2: LITERATURE REVIEW 4

2.1 Tunnel diode 4

2.1.1 Esaki diode 4

2.1.2 Semiconductor double-barrier RTD 6

2.1.3 M-I triple-barrier RTDs 8

2.2 MIM diode 10

2.2.1 Theory and model of MIM diode 11

2.2.2 Point-contact MIM diode 18

2.2.3 Thin film MIM diode 19

2.3 MIIM diode 25

CHAPTER 3: EXPERIMENTAL PROCEDURE 28

3.1 Introduction 28

3.2 Wafer cleaning 28

3.3 Sputtering 29

3.4 E-Beam evaporation 33

3.5 Fabrication 36

3.6 Analytical methods 37

3.6.1 Film thickness measurement... 38

3.6.2 Resistivity measurement 40

3.6.3 Electrical performance measurement.. 41

CHAPTER 4: RESULTS AND DISCUSSIONS 46

4.1 Material selection.. 46

4.1.1 Metal and oxide properties.. 46

4.1.2 Selection of electrodes 48

4.1.3 Tantalum as the electrodes.. 52

4.2 Effects of sputtering pressure on Ta resistivity...................................... 54

4.3 Current –voltage characteristics... 55

4.4 Auto ranging problem 57

4.5 C-V characteristics.. 58

CHAPTER 5: CONCLUSIONS AND FUTURE WORK................................ 70

5.1 Conclusions... 70

5.2 Future work.. 71

REFERENCES 72

LIST OF TABLES

Table 4.1 Properties of oxides.. 46

Table 4.2 Properties of metals.. 48

Table 4.3 Resistance measured by Ohm-meter and Four Point Probe........ 52

Table 4.4 Comparison of refractive index for deposited films and bulk materials.. 53

Table 4.5 Thickness of SiO_2 in sample a and c.. 54

Table 4.6 Range and resolution of the Keithley 196 multimeter................ 58

LIST OF FIGURES

Figure 2.1 Energy band diagrams of tunnel diode 5

Figure 2.2 Band diagrams and I-V characteristics of RTDs 7

Figure 2.3 Operational theories of RTDs 9

Figure 2.4 Band diagram for symmetrical and asymmetrical MIM diodes 11

Figure 2.5 I-V curve and curvature of a typical symmetrical Al-Al2O3-Al diode 13

Figure 2.6 I-V curve and curvature of a typical asymmetrical Ni-NiO-Pt diode 13

Figure 2.7 Theoretical resistance-voltage curves of MIM junctions 14

Figure 2.8 LC characteristics of three plasma oxidized Al-Al_2O_3-Al junctions having different capacitance thickness s_c 16

Figure 2.9 Theoretical resistance-thickness characteristic showing the effect of dielectric constant 17

Figure 2.10 Equivalent circuit model for MIM diode 18

Figure 2.11 Tip of Au-Ni alloy whisker in cat-whisker MIM diode 19

Figure 2.12 I-V characteristics for MIM diodes in micron scale and nanometer scale 21

Figure 2.13 I-V characteristics of Nb/NbO_x/Nb diode in nanoscale 22

Figure 2.14 I-V curve of Al-AlO_x-Pt thin film diode 24

Figure 2.15 I-V curves of MIM diodes with different thicknesses and barrier heights 26

Figure 2.16 Energy band diagram of MIIM on forward bias.................... 27

Figure 3.1 Schematic graph of MIM structure.. 28

Figure 3.2 Schematic diagram of the sputtering process 30

Figure 3.3 Schematic diagram of a planar DC magnetron sputtering system 31

Figure 3.4 Sputtering system BOB 32

Figure 3.5 E-beam evaporation process.. 33

Figure 3.6 E-beam evaporation system (GOMEZ).................................... 35

Figure 3.7 The shadow mask 36

Figure 3.8 Sample fabricated using the shadow mask 37

Figure 3.9 Alphastep 250 profilometer working schematics 38

Figure 3.10 Ellipsometer working process 39

Figure 3.11 Working process of a four point probe.................................. 40

Figure 3.12 Schematic graph of measurement set-up system.................... 42

Figure 3.13 Photo of measurement set-up 43

Figure 3.14 Keithley 4200-SCS model and four-probe station 43

Figure 3.15 Basic test setup for C-V measurement 44

Figure 3.16 Relationship of variables derived from the measurement 45

Figure 4.1 Schematic picture of Al-SiO_2-Cr/Au MIM structure 49

Figure 4.2 I-V curve of Al-SiO_2-Cr MIM structure.................................. 49

Figure 4.3 Schematic figure of resistance before and after breakdown..... 50

Figure 4.4 Resistance for shorted MIM device... 51

Figure 4.5 Structures of 3 samples for optical testing 53

Figure 4.6 The actual structure of deposited samples 54

Figure 4.7 Effects of sputtering pressure on Ta resistivity 55

Figure 4.8 I-V curves of MIM devices with 2 nm of SiO_2 within different voltage ranges 56

Figure 4.9 Cs-Rs of CV sweep for MIM with 8 nm of SiO_2 59

Figure 4.10 Cp-Gp of CV sweep for MIM with 8 nm of SiO_2 60

Figure 4.11 I-V curve of MIM with 8 nm SiO_2 60

Figure 4.12 Cs-Rs of CV sweep for MIM with 5nm of SiO_2 61

Figure 4.13 Cp-Gp of CV sweep for MIM with 5 nm of SiO_2 62

Figure 4.14 I-V curve of MIM with 5nm SiO_2 62

Figure 4.15 Voltage dependence of Capacitance with different thickness of SiO_2 63

Figure 4.16 Voltage dependence of the normalized capacitance of SiO_2 MIMs... 64

Figure 4.17 Cs-Rs of CV sweep for MIM with 2nm of SiO_2 65

Figure 4.18 Cp-Gp of CV sweep for MIM with 2nm of SiO_2 65

Figure 4.19 I-V curve of MIM with 2nm SiO_2 66

Figure 4.20 Leakage current versus SiO_2 thickness at 0.2 volts bias 67

Figure 4.21 $\ln(J/E^2)$ vs. t plots for MIM with different SiO_2 thickness 68

LIST OF SYMBOLS

MIM	metal-insulator-metal
I-V	current-voltage
C-V	capacitance-voltage
E-beam	electron beam
RTD	resonant tunnelling diode
NDR	negative differential resistance
LC	logarithmic conductivity
Φ	barrier height
K	dielectric constant
MIIM	metal-double insulator-metal
BOB	a DC magnetron sputtering system located in the NanoFab
GOMEZ	an E-beam evaporator located in the NanoFab
PVD	physical vapour deposition

CHAPTER 1: INTRODUCTION

1.1 Background

The terahertz frequency region lying between microwave and infrared spectral regions has great promise in both commercial and military applications due to the high switching time and low energy consumption. The metal-insulator-metal (MIM) structure is one of the devices that has been widely explored as mixers, transistors, detectors and other devices for applications such as "through the wall detection" [1] and mobile communication [2]. Devices based on rectifying MIM diodes with a wide variety of material combinations have been developed and investigated such as Ni-NiO-Cr [1], Al-Ta_2O_5-Al [2], Ni-NiO-Ni [3] and Al-Al_2O_3-Al [4].

This research is part of a larger project applying antenna-coupled MIM diodes to a THz detector. My focus is on the evaluation of E-beam evaporated SiO_2 oxide as the insulating layer in MIM device.

1.2 Objective of research

The objectives of this research are as follows:

1.2.1 Selection of materials

Proper metal-insulator combination should be selected considering the dielectric constant, band gap, work function and the availability of the target in the NanoFab where most experiments of this research were carried out. The oxide should have

high band gap and low dielectric constant, while the selection of metal should insure the top electrode doesn't short out with the bottom one due to possible diffusion of metal into the insulator layer. Since only an E-beam evaporator was available for oxide deposition in the NanoFab and only Al_2O_3 and SiO_2 were available on the E-beam evaporator, SiO_2 was selected to be the insulator due to its high band gap and low dielectric constant.

1.2.2 Fabrication of MIM structure

MIM structure should be fabricated using shadow mask. The deposition process of both insulator and metal should be developed and the film quality should be tested and evaluated. The thickness of the insulator needs to be kept under 10nm and the defects should be as few as possible. A uniform and less defective ultra-thin film is the most important part for MIM tunnel junction to work properly.

1.2.3 Characterization of MIM and evaluation of insulating oxide

The electronic properties of the MIM structure should be tested to evaluate performance of the device. Properties such as current-voltage and capacitance-voltage characteristics should be studied. A nonlinear I-V curve is desirable for a tunnel junction to keep a fast response. From these, the SiO_2 as the insulating layer should be evaluated.

1.3 Organization of thesis

This thesis will start with literature reviews of tunnel diodes, MIM diodes and MIIM diodes fabricated by other groups (Chapter 2). Theories, fabrication methods, applications of these diodes and characteristics will also be included.

Then Chapter 3 will detail the experimental techniques and procedures for fabricating and characterizing the MIM structure including the tools used in this process and the reasons for these choices. The results and discussions will be presented in Chapter 4. In this chapter, the current-voltage (I-V) curves and capacitance-voltage (C-V) curves will be given and discussed. The problems that came up during the research will also be discussed. The conclusion of the research and suggestions for future work are contained in the last chapter.

CHAPTER 2: LITERATURE REVIEW

With the rapid development of nanoscale deposition and fabrication technologies, thin films for high speed devices become possible. Tunnel diodes, with the potential for high speed operation, has drawn increasing interest since Esaki invented the first tunnel diode of diode [6]. Since then, many different kinds of tunnel diodes have become available such as resonant tunnelling diodes, metal-insulator-metal diodes and metal-double insulator-metal (MIIM) diodes. These have been explored extensively due to their non-linearity in current-voltage characteristics. This chapter contains theories and operations of tunnel diodes, MIM diodes and MIIM diodes; the studies by other research groups in this area will also be reviewed.

2.1 Tunnel diode

2.1.1 Esaki diode

An Esaki diode is a semiconductor device capable of high speed operation (microwave frequency region) by using quantum mechanical tunnel effects. It was invented in 1958 by Leo Esaki when he discovered the abnormal phenomenon of decreasing current with increasing bias voltage in the current-voltage measurement [6]. He won a Nobel Prize for explaining the operation of this device. Those diodes were heavily doped narrow p-n junctions with the occupied states of the n-region in alignment with the available states of the p-region.

Figure 2.1 shows the typical energy band diagrams and the corresponding I-V curves of a tunnel diode.

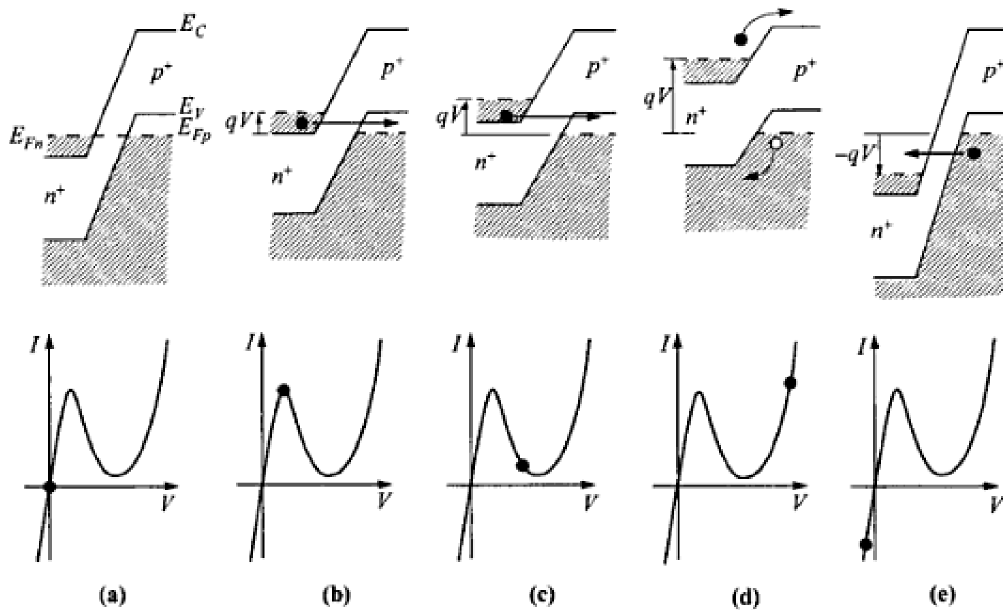

Figure 2.1 Energy band diagrams of tunnel diode [7]

At zero bias, the Fermi levels of n-side and p-side levels up. There's no electrons traveling through, which gives zero current in the I-V diagram. Figure 2.1 (b) shows the situation when a forward bias voltage is applied to the diode. The filled states in the conduction band of the n-side are directly opposite to the empty states in the valence band of the p-side. In this situation, there's a possibility that the electrons in the filled states will directly tunnel into the empty states, yielding a tunnelling current. As the applied voltage continues to increase, the occupied states of the n-side will no longer stay opposite the available states of the p-side. So the number of electrons that can tunnel through reduces, which gives a decreased tunnelling current (see Figure 2.1 (c)). With a further increase of the

applied voltage, the filled state and the empty state are no longer opposite each other, producing zero tunnelling current. As shown in I-V curve of Figure 2.1 (d), the ideal diffusion current will take over. Figure 2.1 (e) shows the situation when reverse bias is applied to the junction. The electrons in the filled state of p-region will tunnel into the empty state of the n-region [7].

The part of the I-V curve presenting a decrease of current with an increase of applied voltage is known as the negative differential resistance (NDR) area [7]. Negative differential resistance is very important for tunnelling devices and other high-frequency applications, because the tunnelling action occurs so fast that there is no transit time effect and therefore no signal distortion.

2.1.2 Semiconductor double-barrier RTD

Resonant tunnelling diode (RTD) is a device that utilizes quantum effects to achieve current-voltage characteristics with a NDR region. RTDs are of great interest because of their potential for high speed operation and low power consumption which can be carried out in the nanoscale. They emerged as a pioneering device in the field in the middle of 1970s after Esaki and Tsu proposed the idea of resonant tunnelling in 1973 [8]. Figure 2.2 depicts the band diagram of a typical double-barrier RTD. The dots on the current-voltage curve correspond to the band diagrams. A RTD typically consists of a thin, undoped quantum well layer sandwiched between two thick, undoped barriers and heavily doped emitter and collector.

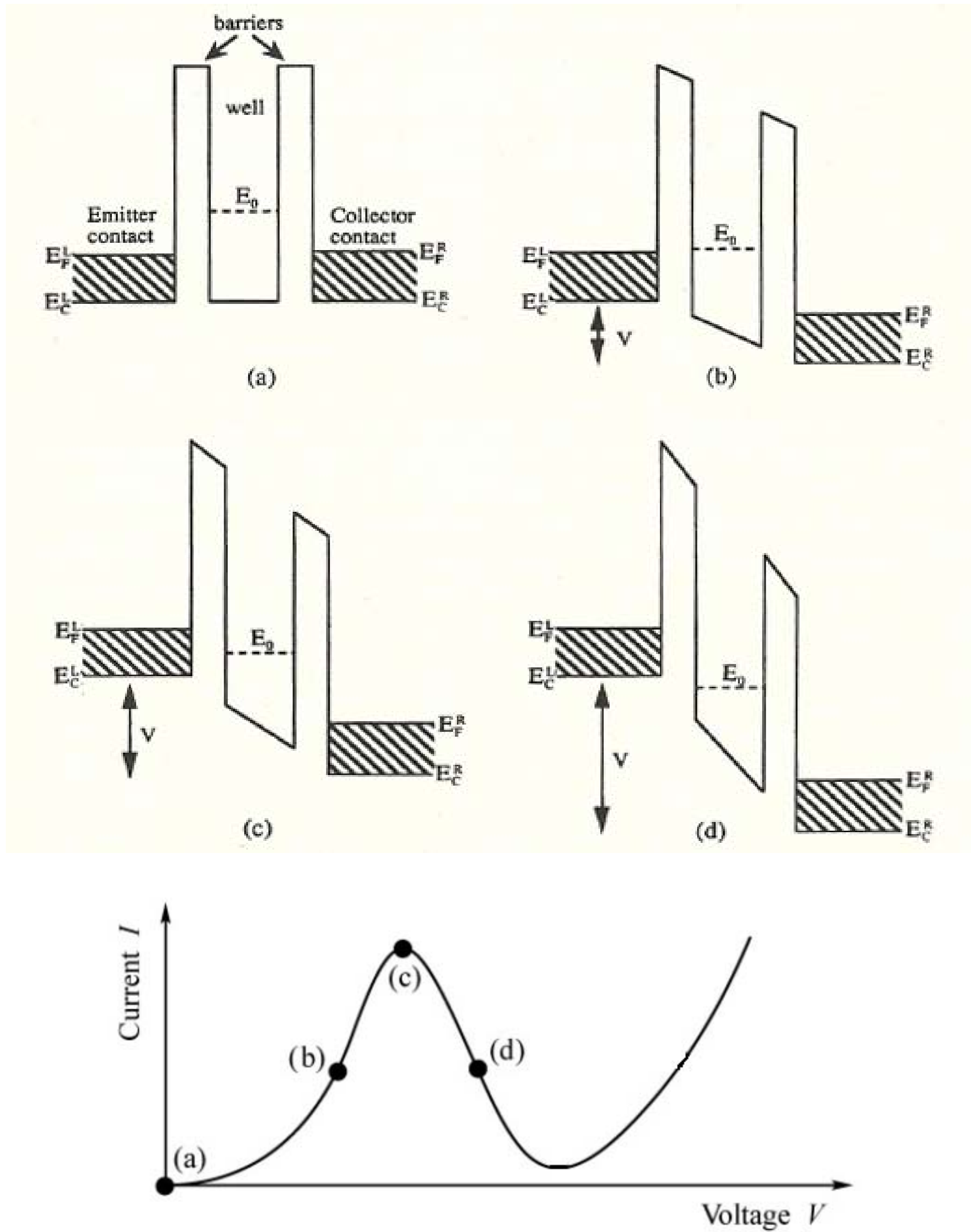

Figure 2.2 Band diagrams and I-V characteristics of RTDs [9]

At zero bias, shown in Figure 2.2 (a), there is no electron traveling through the double barriers. As the bias voltage increases, the energy of electrons flowing from the emitter coincides with the energy E_0 in the quantum well (Figure 2.2 (b)

at threshold bias). The electrons then are capable of tunnelling through the barriers and reaching the collector on the other side, thus creating a tunnelling current shown by dot (b) on the I-V curve. As the increase of the bias voltage continues, the numbers of electrons traveling through the barriers increases continuously to a maximum. When the E_0 falls below the conduction band of the emitter, the electrons cease to flow through the barriers and the current will decrease as shown in Figure 2.2 (d) [9].

A resonant tunnelling diode (RTD) belongs to the family of tunnel diodes but is different from the regular Esaki diode. A RTD usually contains two potential barriers creating a quantum well sandwiched between them, therefore the I-V characteristics with positive and reverse bias are symmetric. The Esaki diode, on the other hand, uses heavily doped p-n junction which has different I-V curves with positive bias and reverse bias. Besides, the Esaki diode has high capacitance while the RTD has a variable capacitance with bias voltage [9,10].

2.1.3 M-I triple-barrier RTDs

T. Suemasu et al. fabricated a metal ($CoSi_2$)/insulator (CaF_2) triple-barrier resonant tunnelling diode in 1993 [11]. The negative differential resistance can usually be observed in regular semiconductor double-barrier RTDs. But in the metal-insulator heterostructure diode that has metal instead of semiconductor as the source layer, a triple-barrier structure becomes necessary. Figure 2.3 shows the operational principles of both the double-barrier structure and the triple-barrier structure. From Figure 2.3 (a), the double-barrier M-I diode has a very non-linear

current-voltage characteristic due to the resonance. However, no NDR was observed in the I-V graph because after the Fermi energy of the emitter aligns with the quantized level in the quantum well, the resonance conditions are still satisfied despite the increase of the bias voltage. Therefore, only a rapid increase of current was observed. However, for triple-barrier structure shown in Figure 2.3 (b), resonance only occurs when the Fermi energy of the emitter exceeds the quantized levels in both quantum wells which align with each other at the same time [11].

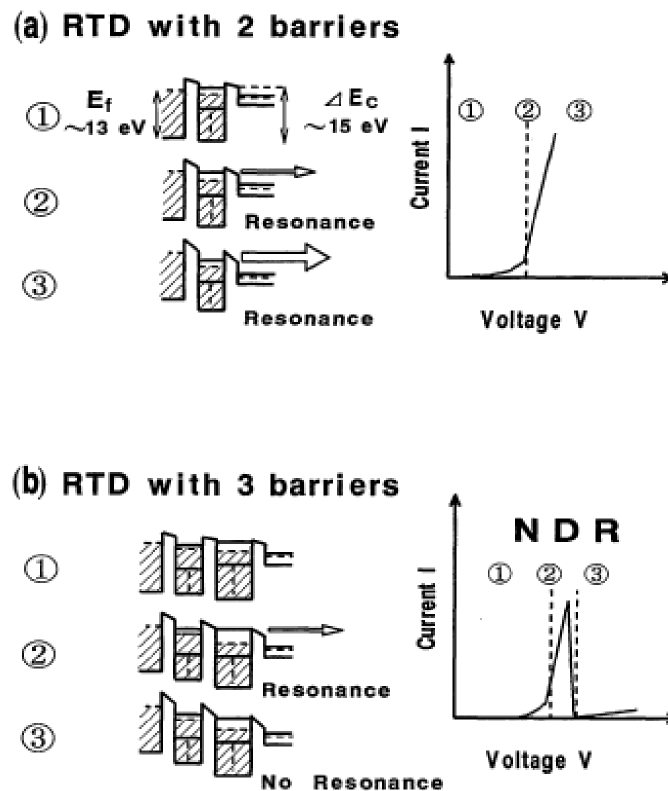

Figure 2.3 Operational theories of RTDs [11]

The most important characteristic of a RTD is the high speed that is determined primarily by the quantum-mechanical tunnelling time and the circuit charging

time. Since the tunnelling time decreases with smaller barrier layer thicknesses and barrier heights [12], T. Suemasu et al. made the triple barriers (CaF_2) of this RTD as thin as 0.9 nm. An epitaxial method was employed for the growth of metal-insulator multilayer, because both $CoSi_2$ and CaF_2 have fluorite lattice structures and lattice mismatch of only -1.2% and 0.6% to Si respectively. A peak/valley ratio of 2-3 was obtained at 77 K and a ratio as high as 2 was achieved at 300 K in this research. The dependence of resonance voltage on the quantum well thickness was also investigated by T. Suemasu et al. in this paper. The results agree well with the theory that the resonance voltage decreases with the increasing quantum well thickness. [11]

2.2 MIM diode

A metal-insulator-metal diode, also known as metal-oxide-metal (MOM) diode or metal-barrier-metal (MBM) diode, is a device with a thin layer of insulator sandwiched between two metal electrodes. If the insulating layer is sufficiently thin, current can flow between the two electrodes by means of the tunnel effect [13]. MIM diodes coupled with antennas, which can rectify high frequency antenna current induced by incident radiation, are of great promise since high quality imaging systems need fast and sensitive detectors. Besides, these devices can operate at room temperature which is different from the semiconductor-based detectors [14].

2.2.1 Theory and model of MIM diode

The diode characteristics of the MIM structure are due to quantum mechanical tunnelling of electrons through insulating films between two metals. This was first considered by Frenkel in 1930 [15] and was further developed by Stratton [16] and Simmons [17]. The band diagram of symmetrical and asymmetrical MIM diodes is shown in Figure 2.4. When two metallic electrodes are separated by an insulating layer, the top of the energy gap of the insulator needs to be above the Fermi level of the electrodes to reach equilibrium. Therefore, a potential barrier between the two electrodes impeding the flow of current between them was introduced.

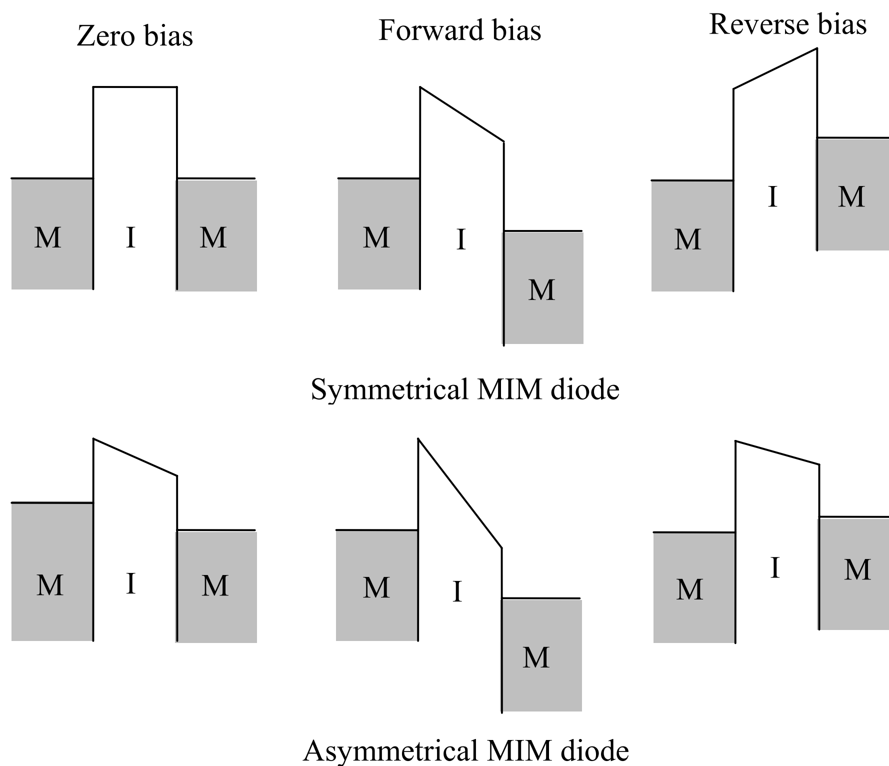

Figure 2.4 Band diagram for symmetrical and asymmetrical MIM diodes

There are two ways for the current to flow across the insulating layer. Either the electrons have enough thermal energy to get over the barrier or the barrier is thin enough for the electrons to penetrate through by the tunnel effect [17]. At room temperature, thermal current can be neglected and the tunnel effect becomes dominant. For the symmetrical MIM diodes, current flows in either direction at zero bias. When a bias voltage is applied, positive or negative, the current flows across the insulating layer to the electrode on the other side. MIM diodes with dissimilar electrodes demonstrate asymmetry and sufficient non-linearity [1]. The asymmetry is shown in Figure 2.4. At zero bias, current flowing across the insulator is allowed. This is due to the different work functions between the two electrodes. Unlike the symmetrical MIM diodes, the asymmetrical MIM diodes have different current-voltage characteristics for the forward bias and reverse bias. The average barrier height with forward bias is much lower than with the reverse bias, therefore the tunnel probability is much higher [18].

Figure 2.5 and 2.6 show the I-V curve and curvature coefficients for the typical symmetrical and asymmetrical MIM diodes. The curvature coefficient is the ratio of the second derivative to the first derivative [19]. It can be seen from the graphs that the asymmetrical MIM diode exhibits a higher non-linearity than a symmetrical diode. Al-Al_2O_3-Al MIM diode demonstrates a peak curvature coefficient of -13 V^{-1} and a zero-bias curvature coefficient of -3 V^{-1} while Ni-NiO-Pt diode exhibits a peak curvature coefficient of around 1.5 V^{-1} and a zero-bias curvature coefficient of almost zero. Although the asymmetrical diode finds

desirable applications in energy harvesting, the symmetrical MIM diode can still attract many interests with fair non-linearity.

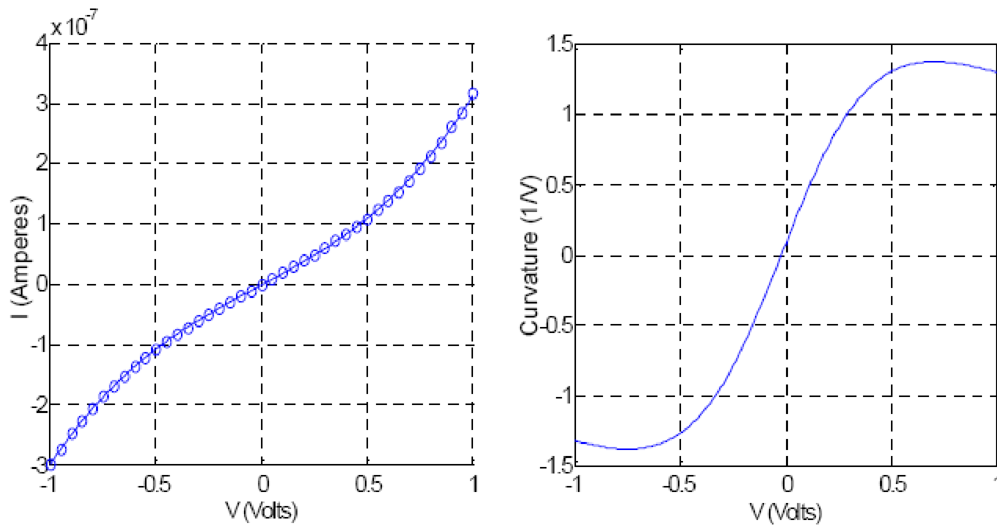

Figure 2.5 I-V curve and curvature of a typical symmetrical Al-Al2O3-Al diode [19]

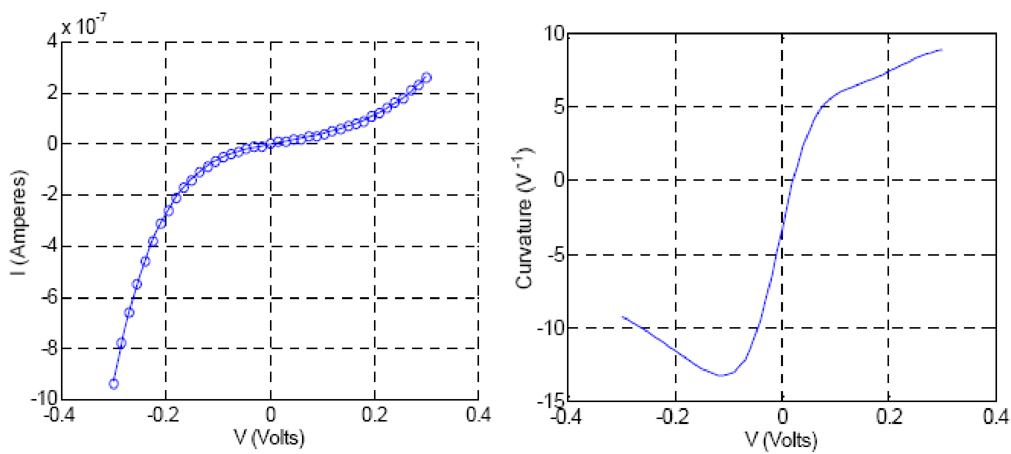

Figure 2.6 I-V curve and curvature of a typical asymmetrical Ni-NiO-Pt diode [19]

The electric tunnel effect for MIM junctions was theoretically investigated by J. G. Simmons as early as 1963 [17]. Figure 2.7 shows the theoretical tunnel resistance-voltage characteristic of MIM junctions with a rectangular barrier. This is for an ideal MIM diode without image forces and tunnel resistivity is V/J. It is observed

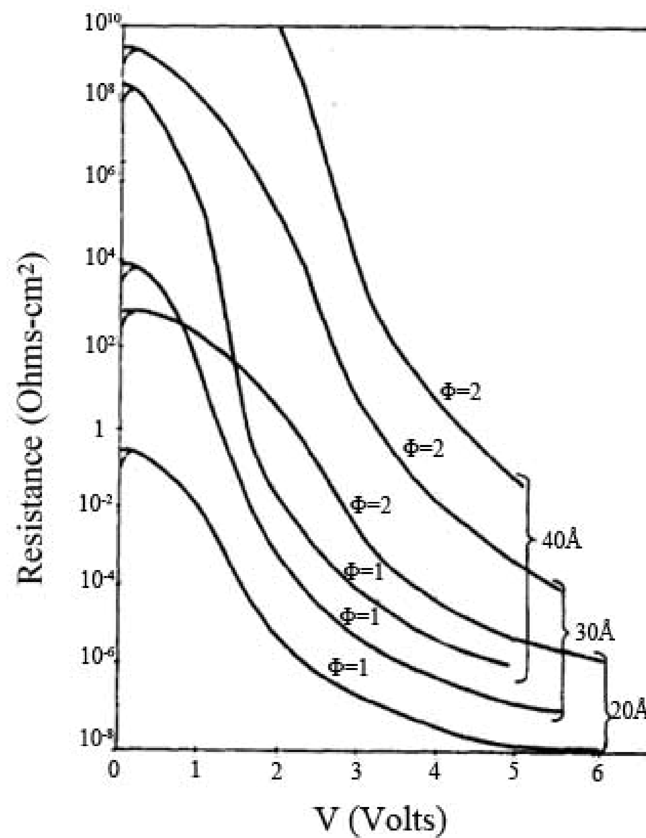

Figure 2.7 Theoretical resistance-voltage curves of MIM junctions [17]

from the graph that with constant voltage and barrier thickness, the tunnel resistance increases with the increasing barrier height (Φ). With the same barrier height and applied voltage, a lower resistance can be obtained with lower barrier thickness. For 2 V of barrier height, the resistance reduces almost 100 times as the

barrier thickness drops by 1 nm, and resistance drops quickly with the increase of the bias voltage. So if a device needs low resistance, efforts can be made to choose proper material combinations to reduce the barrier height or minimize the barrier thickness. Usually, the detectors need to work under lower voltage in which region the tunnel resistance is relatively high. Therefore, the insulating film needs to be kept thin by adopting new techniques.

As for how to obtain the barrier height of MIM diodes, efforts have also been made in this field. Gundlach and Hölzl obtained the barrier height of Al-Al_2O_3-Al tunnelling junctions using logarithmic conductivity (LC) method in 1971 [20]. The LC characteristic was achieved by plotting the logarithmic derivative of tunnel current density ($\frac{d \ln J}{dV}$) against applied voltage (V) and barrier height was found according to the position of LC maximum. They compared their results to those found from photoelectric measurement and the results were in good agreement.

Figure 2.8 shows the logarithmic conductivity characteristics of Al-Al_2O_3-Al tunnelling junction obtained by Gundlach and Hölzl. From Figure 2.8, barrier heights of Al-Al_2O_3-Al Φ_1 and Φ_2 can be achieved from the position of the logarithmic conductivity maxima at 2.3 eV and 1.85 eV respectively. According to their study, the LC characteristic is typical for tunnel current in MIM junctions.

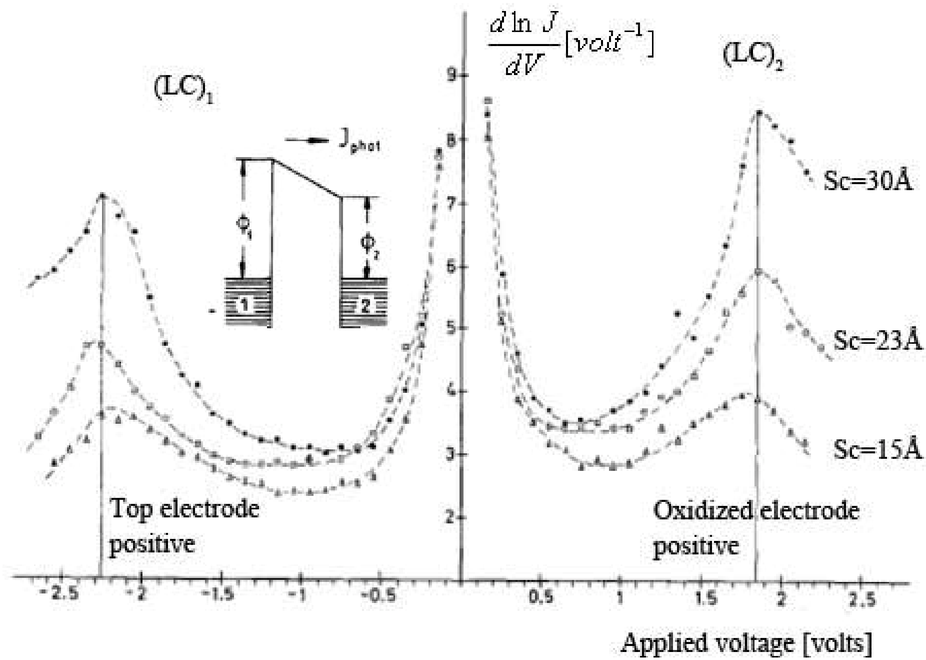

Figure 2.8 LC characteristics of three plasma oxidized Al-Al_2O_3-Al junctions having different capacitance thickness s_c [20]

The tunnel characteristics of MIM junctions also depend on the dielectric constant of the insulating film. Figure 2.9 illustrates the effect of the dielectric constant (k) on the tunnel resistance [17]. From the graph it can be seen that a smaller dielectric constant, K, yields lower tunnel resistivity and the tunnel resistance decreases as insulating film becomes thinner. This agrees with the conclusion from Figure 2.7. Simmons also stated that for dielectric thickness of less than 4nm, tunnelling is the dominant way for the rectification. However, for dielectric thickness of more than 4nm, either thermionic emission or tunnelling is the possible dominant way depending on the barrier height and the bias voltage [21].

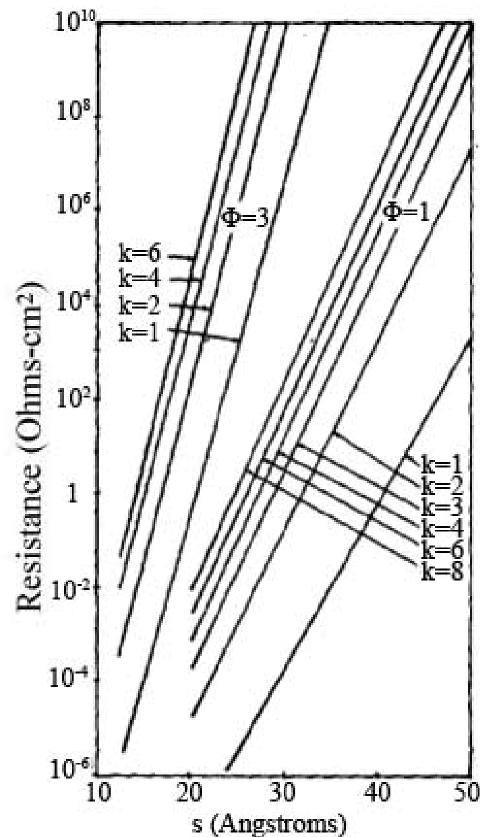

Figure 2.9 Theoretical resistance-thickness characteristic showing the effect of dielectric constant [17]

Figure 2.10 shows the equivalent circuit model for a MIM diode as a combination of resistance and capacitance. Resistance includes spreading resistance (R_S) and tunnelling resistance (R_T), and C is the junction capacitance. The fixed resistor and non-linear resistor connect to the capacitance in parallel. The non-linear resistor is responsible for the rectification of the captured signal. The capacitance needs to be kept small to minimize the losses caused by current flowing through the capacitor. Also, the frequency of operation can be increased by reducing the capacitance. There are two ways of reducing the capacitance: a) increase the thickness of the insulating film, and b) minimize the contact area of the MIM

structure. However, the probability of tunnelling drops significantly when the thickness of the insulating film exceeds 5nm [18]. So it is better to reduce the contact area of the MIM diode.

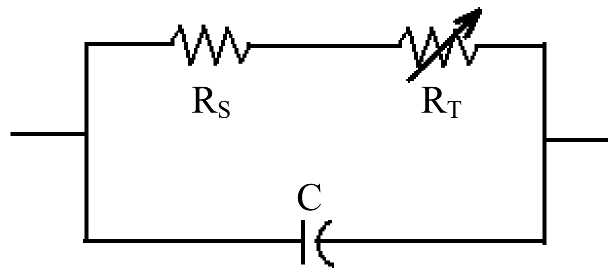

Figure 2.10 Equivalent circuit model for MIM diode

2.2.2 Point-contact MIM diode

MIM diodes originally existed as point-contact MIM diodes, also known as "cat-whisker" diodes, which became the fastest electronic devices operating by 1970s. It allows the extension of microwave techniques into sub-millimeter and infrared spectrum region [22].

The point-contact MIM diode was formed by pressing the sharp tip of a thin metal whisker (see Figure 2.11) acting as a long wire antenna against a metal plate, with the native oxide as the insulating layer. In this case, the radius of the whisker tip determines the contact area of the MIM diode, which is estimated to vary from 0.02 μm^2 to 0.1 μm^2 [23].

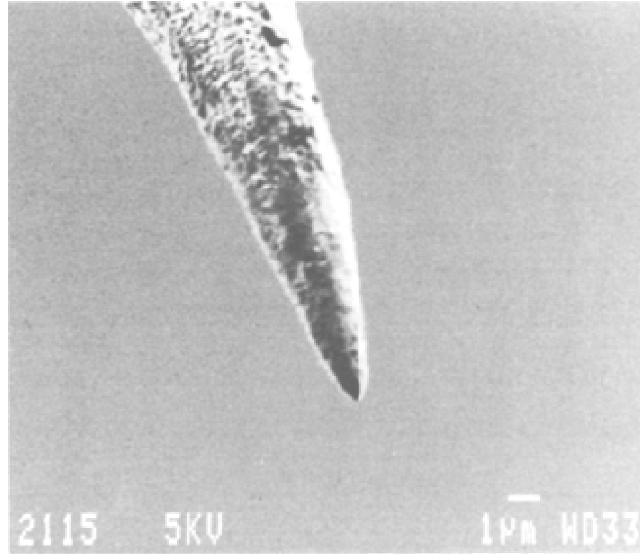

Figure 2.11 Tip of Au-Ni alloy whisker in cat-whisker MIM diode [23]

Point-contact MIM diodes were first utilized for detection and mixing at sub-millimeter wavelengths in 1966 [24]. In later years, detections in the infrared and optical range were made with point-contact MIM diodes [25, 26]. Their ultrafast rise time kept them in use for many years in many applications of high frequency rectification ranging from GHz to 150 THz [27, 28]. Despite their success, the point-contact MIM diodes are not suitable for commercial use, but are only restricted to laboratory application. Unstable responsivity is one of the problems. Point-contact MIM detectors also have problems of micro-phony and electrical transients. As well, the characteristics of the diodes are not easily reproduced due to the fact that the contact area and insulator thickness are difficult to control [22].

2.2.3 Thin film MIM diode

Since operation of point-contact MIM diodes has so many difficulties, the thin film MIM diodes have attracted interest. With the development of

photolithography, it's possible to fabricate stable and reproducible thin film MIM structures [29]. Many studies have been done on the thin film MIM diodes [4, 22, 30-31]. However, the thin film MIM diode detectors in the early stage of development actually had a lower detectivity than point-contact MIM diodes due to the larger contact area [32]. Efforts have been made to downsize the contact area of MIM diodes.

I. Wilke et al. fabricated a Ni-NiO-Ni thin film diode to detect 10.6 μm CO_2 laser radiation (up to 30THz) in 1994 [33]. The Ni and NiO films were deposited by plasma sputtering and the diode was fabricated by using electron-beam direct-writing lithography. The thickness of the insulating layer was monitored by a quartz crystal oscillator and measured by Rutherford Back Scattering to be 33Å. This MIM diode had the smallest contact area of 0.056 μm^2 at that time. Non-linearity of the diode, which was comparable to that of the point-contact MIM diodes, was demonstrated by measuring the second derivative of the current-voltage characteristics. Two factors were considered to contribute to the non-linearity: electron tunnelling and spreading resistance due to pinholes in the insulating layer. They attributed the non-linearity primarily to electron tunnelling because the second derivative of the current-voltage characteristics increases significantly with the decrease of the zero-bias resistance [33].

B. Berland tried to reduce the contact area from the micron scale to the nanoscale. MIM diodes were fabricated with contact area of 10 μm×10 μm and 50 nm×50

nm, tested and compared [19]. Figure 2.12 shows the typical current-voltage characteristics for MIM diodes in the micron and nanometer scales. The micron scale device, shown in the left graph, exhibits higher non-linearity and high degree of asymmetry while the nanoscale device, shown in the right graph, demonstrates characteristics of a resistor. Among the 12 diodes B. Berland made

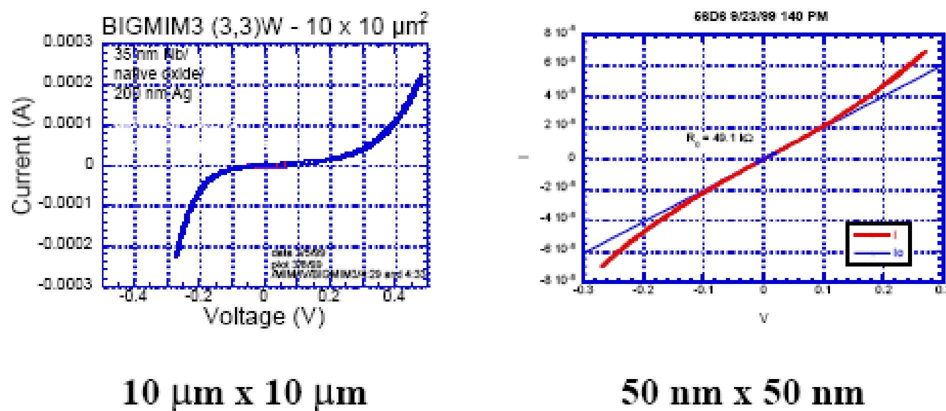

Figure 2.12 I-V characteristics for MIM diodes in micron scale and nanometer scale [19]

on the same chip the resistance of the nanometer diode varied from one to another. The performance of a device is evaluated based on non-linearity, impedance of the device and reproducibility and uniformity of the fabrication. Non-linearity, which was defined by $\frac{dI}{dV} \cdot \frac{V}{I}$, is roughly estimated to be greater than 3 in order to get measurable conversion efficiencies. The impedance should be matched to the antenna. The diodes on the chip should be uniform and reproducible [19]. More effort was made in this area by B. Berland. He fabricated Nb/NbO_x/Nb thin film diodes in nanometer scale and reduced the contact area gradually. The metals were deposited by means of an ion-beam system with an ion gun for deposition

and an additional gun for milling; the oxide layer was deposited by using plasma oxidation that exposes the base metal electrode to an O_2/Ar environment. And the results were more favourable (see Figure 2.13). As can be seen from the graph,

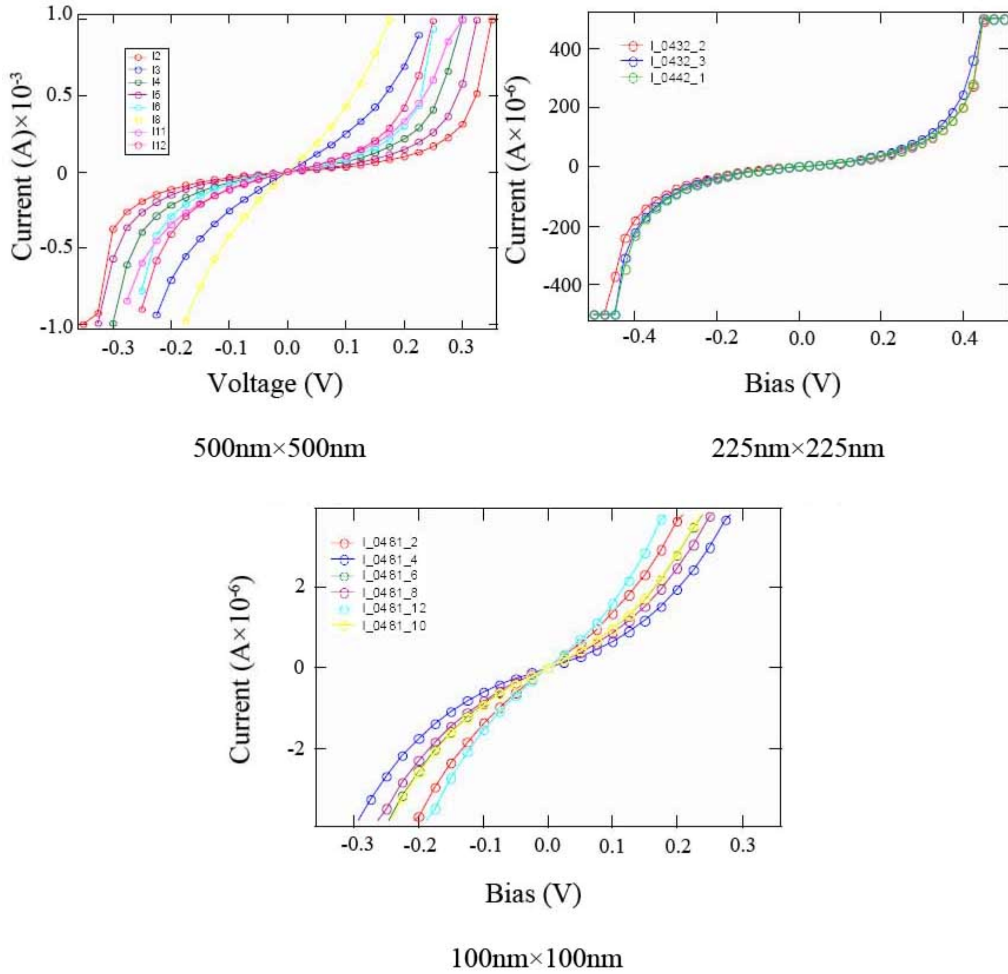

Figure 2.13 I-V characteristics of Nb/NbO_x/Nb diode in nanoscale [19]

the nanometer device exhibited a higher non-linearity calculated to be greater than 3. The devices also demonstrated relatively low impedance and fair reproducibility [19].

Krishnan et al. believed that MIM diodes with dissimilar electrodes exhibit enough non-linearity and asymmetry without external bias. They made improvements to the Ni-NiO-Ni diode by using Ni and Cr electrodes, which have a work-function difference of 0.65 eV, as the electrodes in 2008 [1]. Two detectors with different contact areas of 100 μm^2 and 1 μm^2 were produced and tested in this research. The metal electrodes were deposited using DC sputtering system. The insulating layer was deposited through a controlled plasma oxidation process at a very low power and O_2 was introduced together with Ar. In this oxidation process, the Ar-O_2 gas ratio and oxidation time are very important. For Ar-O_2 ratio of 1:1, the film roughness measured by AFM is almost the thickness of the film, while the Ar-O_2 ratio of 2:1 gave relatively low roughness. After 10 minutes, the oxidation time didn't increase the film thickness further, but improved the uniformity of the film. The tunnel current increased from 1.5nA to 0.8nA with the decreasing thickness of the insulating layer and the contact area. The asymmetry (ratio of forward current to reverse current) as high as 4.5 and 6 were obtained for the diodes with large contact area and small contact area respectively [1].

Recent research on Al-AlO_x-Pt thin film diodes has been done by B. Tiwari et al [34]. This device can operate at 30 THz. A work-function difference of 1.4 eV made Al and Pt good choice for electrodes. The contact area of this MIM thin film diode is 50×80 nm^2. A new procedure for fabrication was designed in this process. The MIM structure was deposited using an E-beam evaporation system. Unlike a

regular E-beam system, the evaporation system in Tiwari's research had an ion gun, which was used for in situ etching. After the bottom electrode Al was deposited, the evaporator was vented to the atmosphere and a thin layer of native oxide formed immediately. This layer of native oxide had poor quality. Therefore, the Ar plasma was used to remove the native oxide layer and gave a layer of clean Al. Then Al oxide was grown by the process of controlled oxidation of Al, which yielded a uniform and high-quality oxide layer. Oxygen pressure and oxidation time are the primary control parameters for the in situ oxidation process. The top electrode was evaporated following the oxidation process without breaking the vacuum [34]. The current-voltage characteristics of this diode are shown in Figure 2.14.

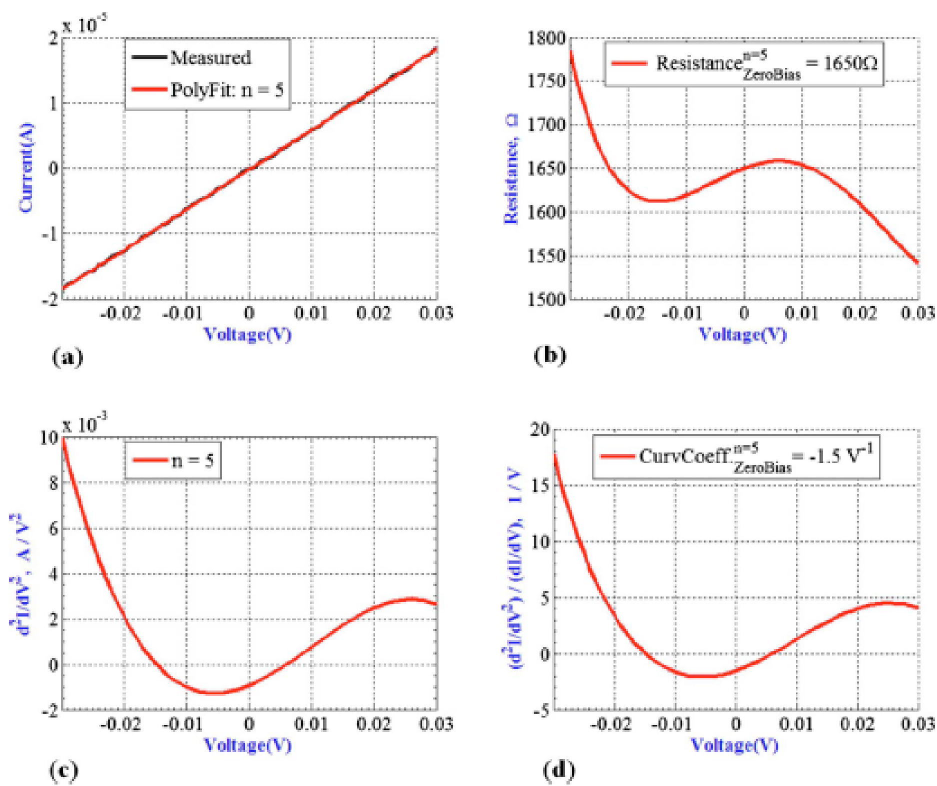

Figure 2.14 I-V curve of Al-AlO_x-Pt thin film diode [34]

Current-voltage characteristics were measured within the range of -0.03 V to 0.03 V because the dielectric layer was very thin (estimated to range between 2 nm and 3.5 nm). Figure 2.14 (a) shows the I-V response of the device and a fifth-order polynomial fit. Although the polynomial fit of the I-V curve is almost linear, the measured I-V response was not smooth at all. Therefore, great non-linearity was observed in Figure 2.14 (c). And the maximum curvature coefficient as high as 18 occurs at -0.03 V, as can be observed from Figure 2.14 (d) [34].

2.3 MIIM diode

For a diode rectifier to operate efficiently at high frequency levels, both sufficiently non-linear I-V characteristic and high on-state conductivity are required. However, the simple MIM can not have both nonlinearity and conductivity at the same time. Thicker and higher barrier MIM diodes exhibiting more non-linearity while thinner and low barrier ones showing more conductivity (see Figure 2.15) [5]. Therefore, a MIIM device has been drawing attention due to the existence of a triangular quantum well on forward bias as shown in Figure 2.16. Phiar Corporation [5] has fabricated a MIIM diode which operates at less than 10 THz. However, no details were revealed in their paper about the material combinations used. Phiar also came up with new structures such as a MIIMIM hot electron tunnelling transistor. These devices hold promise for higher operating speed.

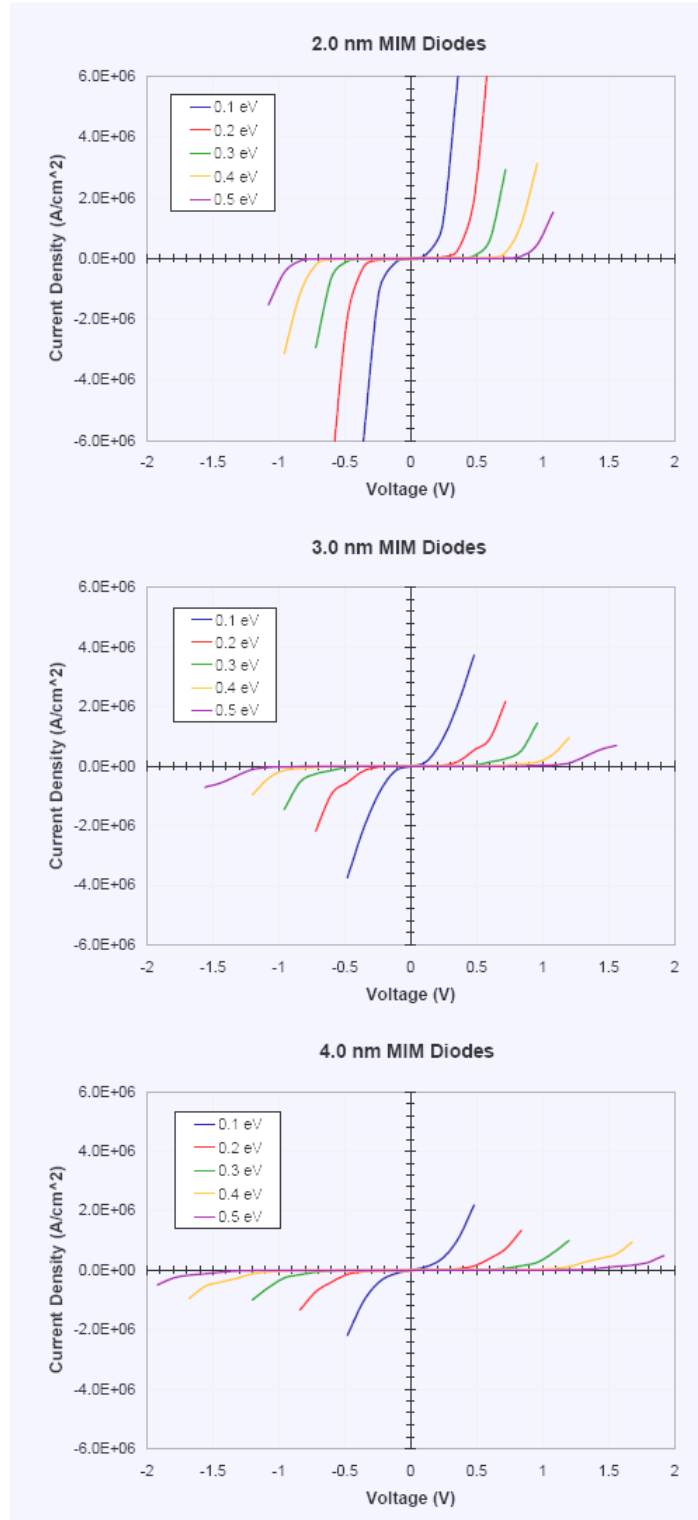

Figure 2.15 I-V curves of MIM diodes with different thicknesses and barrier heights [5]

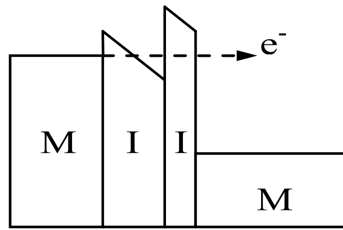

Figure 2.16 Energy band diagram of MIIM on forward bias [5]

CHAPTER 3: EXPERIMENTAL PROCEDURE

3.1 Introduction

In this study, a MIM structure schematically shown in Figure 3.1 needed to be fabricated to test electrode-insulator combinations. Evaluations of the structure were carried out to study its electrical performance. To this end, we needed to clean the wafers, sputter metal electrodes, deposit insulating layers using E-beam evaporation, fabricate the whole structure, and analyze the film qualities and device performance.

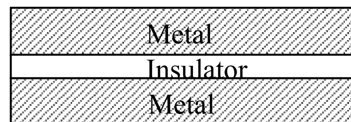

Figure 3.1 Schematic graph of MIM structure

3.2 Wafer cleaning

Silicon wafers are usually covered with different kinds of debris, such as foreign particles (dust, clothing particles, bacteria, etc.), contaminants (skin, oil, ions) and native silicon oxide. Before Si wafers can be used as substrates they must be cleaned to remove these surface contaminations. A piranha cleaning solution was used to remove organic and metallic containments from the wafer surface. The piranha solution consists of a mixture of H_2SO_4 and H_2O_2 at volume ratio of 3:1. The cleaning was done in the NanoFab clean room on a wet bench with adequate ventilation. This process, however, cannot remove the native oxide on the wafer

surface. This native oxide can either be removed by using diluted hydrofluoric acid on the wet bench in the clean room or by in-situ plasma clean. In our case, the native oxide has no significant effects on the performance of the device. Therefore, only the piranha clean was needed in this study. It is important that the wafer is cleaned just before being used to reduce possible contamination. If it has to be stored for a while, it was kept in a sealed box in the clean room. Under certain circumstances, microscope slides were used as the substrate for sputtering. In that case, the microscope slides were cleaned by using isopropanol and ethyl alcohol.

3.3 Sputtering

Sputtering is one of the most widely used physical vapour deposition (PVD) methods for depositing films, which facilitates the transfer of atoms from a solid source onto a substrate. In a sputtering deposition, argon (Ar) is introduced into an evacuated chamber. The Ar is the working or sputter gas. When a sufficiently high DC voltage is applied between the two electrodes at a reduced gas pressure, the gas can be ionized and a plasma forms. Because of the magnet array located under the cathode, the formed Ar plasma is trapped close to the target. Magnetron sputtering is based on the generation of this magnetically enhanced glow discharge. During the sputtering process, Ar is continuously fed to maintain a constant chamber pressure. The positively-charged ions of Ar^+ are then accelerated toward the negatively charged target at high speed by the imposed electric field. The Ar^+ ions bombard the target and sputter the neutral atoms off the target source, which then transit through the plasma and condense onto the

chamber walls and substrate. The atoms nucleate on the substrate and gradually coalesce into a continuous film [35]. This process is shown schematically in Figure 3.2 below. The plasma can be sustained in a lower pressure because the secondary electrons are emitted as the Ar^+ strike the target surface. The secondary electrons are accelerated into the plasma and ionise the gas atoms leading to generation of new ions. These secondary electrons are also trapped close to the target surface by the magnetic field [36].

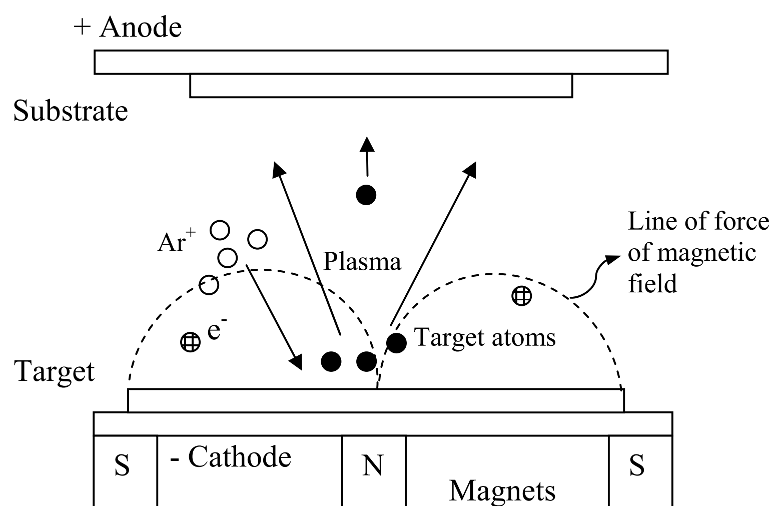

Figure 3.2 Schematic diagram of the sputtering process

For the experiments in this study, a DC planar magnetron sputtering system was used. The system, known as BOB, is located in the NanoFab of Electrical and Computer Engineering. A schematic diagram of this system is shown in Figure 3.3.

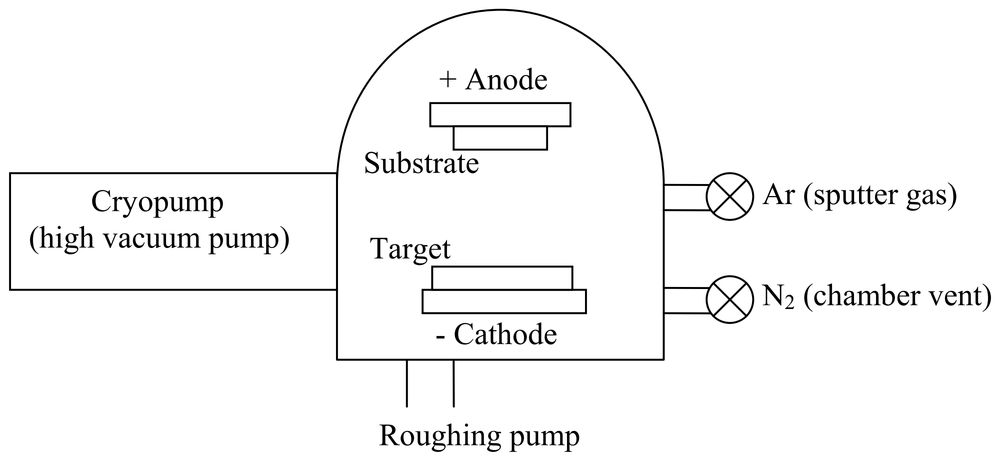

Figure 3.3 Schematic diagram of a planar DC magnetron sputtering system

The system is usually kept under vacuum when it's not being used. In order to open the chamber, the chamber vent is opened to allow N_2 flow into the chamber, so that the chamber pressure can be increased to atmospheric pressure. Then the chamber top can be raised up mechanically. The system used in this study is a sputter-up system. The substrate was held to the holder located at the top of the chamber. The substrate was applied with the positive voltage (or grounded) while the target at the bottom of the chamber was connected to the cathode. The system was pumped to base pressures of $\sim 10^{-6}$ Torr using a roughing pump and a high vacuum cryopump. During sputtering, Ar was introduced into the chamber through a mass flow controller, and the gate on the high vacuum pump can be throttled to reduce the pumping speed and held to achieve the desired sputtering pressures.

Figure 3.4 shows the picture of this sputtering system BOB. During a typical process in this study, the chamber was pumped down to a base pressure of 2.4×10^{-6} Torr and the typical sputter pressure was 6 mTorr. The targets used were 3" diameter, and typically 99.95% pure. Many metal targets are available in the NanoFab, such as Ta, Cr, Al, Ni, Nb, Au, etc. The target was cleaned by being pre-sputtered for 3 min at 7 mTorr with the gun shutter closed. Then the gun shutter was opened and the metal was sputtered onto the clean Si wafer. Typical deposition conditions included DC power of 300 W and deposition rate of 8 nm/min. During deposition, the substrate was constantly rotated to get a uniform film.

Figure 3.4 Sputtering system BOB

3.4 E-Beam evaporation

E-beam evaporation is a physical vapour deposition (PVD) method using a stream of electrons to heat and evaporate the source material. It can deposit both metals and dielectric materials. If the evaporation voltage exceeds 10kV x-rays can be produced causing radiation in the test samples. Although the evaporation process has this possible drawback, it can produce a uniform and thin film. A quartz crystal monitor inside the chamber allows the film thickness to be calibrated [35]. Figure 3.5 shows the typical E-beam evaporation process.

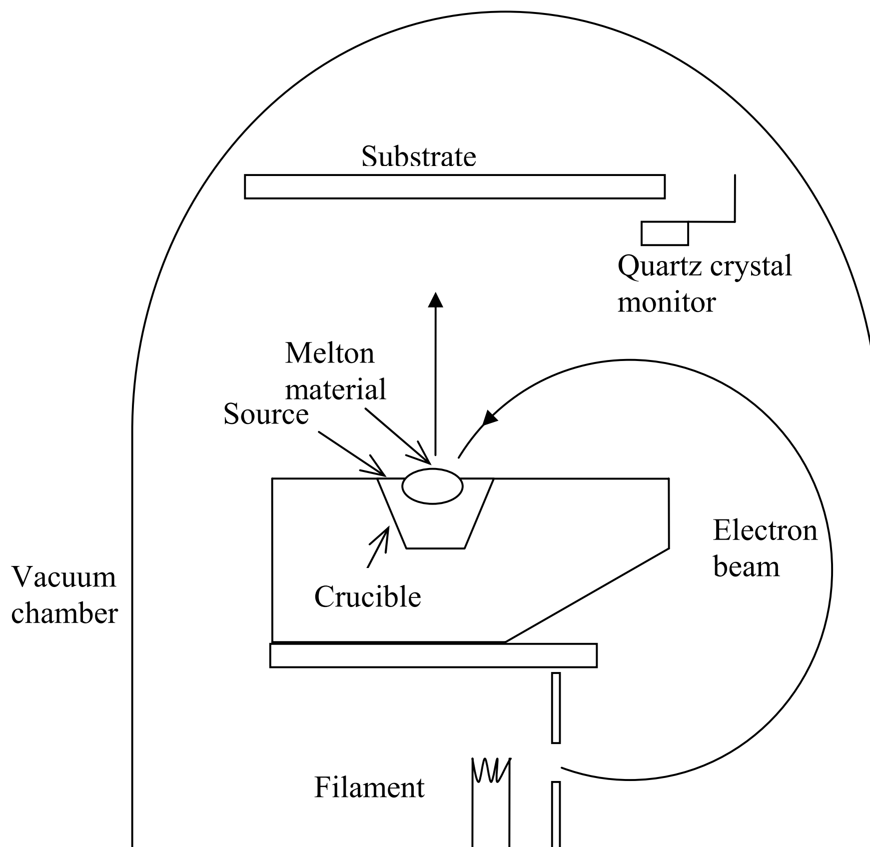

Figure 3.5 E-beam evaporation process

The E-beam evaporation contains a water cooled crucible holding the target source. And on the side of the crucible, there is a filament which produces electrons when high current passes through it. The electrons are accelerated and bent 180° by a magnet so that they strike the center of the crucible. The high energy melts the target source and the target material then evaporates from the crucible onto the substrate in the holders at the top of the chamber. The water cooling mechanism keeps the outer side of the target in solid state thus preventing the contamination from the crucible.

The E-Beam evaporation takes place inside the evacuated chamber which contains shutters, wafer holders, a quartz crystal thickness monitor and the target. The evaporation is required to be carried out under high vacuum in order to grow uniform films. When the chamber pressure drops sufficiently, the mean free path of the coating atoms will exceed the diameter of the chamber, which ensures that the coating atoms hit the substrate before they collide with each other causing un-non-iformity of the film.

The deposition rate is important for the precise control of film thickness. For very thin films ranging from 1 nm to 10 nm, a low and steady rate deposition is needed to get high quality films. The deposition rate can be monitored by the rate monitor and controlled by the adjusting the emission current and beam position. The thickness of the film can be monitored by the quartz crystal below the substrate.

Since the quartz crystal is not at the same height as the substrate, a tooling parameter is needed to calibrate the thickness.

Figure 3.6 shows the electron beam evaporation system, known as GOMEZ, used in this study. It is located in the NanoFab in the Electrical and Computer Engineering department. The chamber was evacuated to the pressure of 1.0×10^{-6} Torr before evaporation begins. SiO_2 thin films were deposited at an emission rate of 0.5mA, and tooling factor of 80%. The density and Z-factor used for the deposition was 2.2 and 1.07, respectively. The deposition rate is controlled steadily at 0.5 Å/s before opening the shutter and throughout the whole deposition process.

Figure 3.6 E-beam evaporation system (GOMEZ)

3.5 Fabrication

Usually, the device can be fabricated to produce a diode by the process of design, deposition, photolithography and lift-off. This, however, takes time and is costly, especially at the early phase of the study when the exact materials combination is not yet determined. Therefore, multiple simple devices were fabricated by using a shadow mask with holes of 5 mm in diameter on it as shown in Figure 3.7.

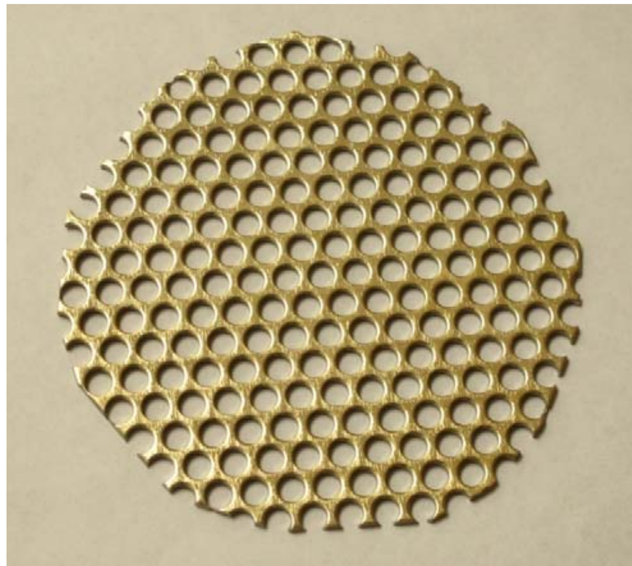

Figure 3.7   The shadow mask

This mask was used for depositing the top electrode of Ta and Au. When making a MIM diode, it's generally assumed that the deposition of thin films and the contact area are the two major factors that affect the characteristics of the diode [18]. The contact areas of the diodes made by other groups are much smaller than that of the MIM junction in this study. This means that the MIM junctions in this study will have a higher leakage current at the same bias voltage due to the film

defects and the large contact area. Therefore, if the test of this MIM junction can give satisfactory results, diodes with smaller contact area could be made to get better performance. The sample fabricated using a shadow mask is shown in Figure 3.8.

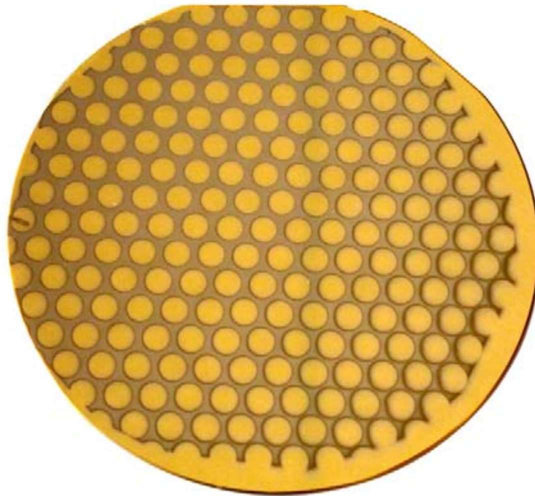

Figure 3.8 Sample fabricated using the shadow mask

3.6 Analytical methods

For the MIM structure to work properly, high quality films must be deposited. Film thickness and sputtering recipe optimization must be done. These tests and analysis were done prior to the fabrication of the device. The thickness and resistivity measurements were all done on test glass wafers to get the proper parameters and recipe. The electrical performance of the structure was also evaluated using I-V tests.

3.6.1 Film thickness measurement

Film thickness control is important since the films deposited in this study are as thin as several nanometers. The thickness of the metal and the insulator in the MIM structure are measured with two instruments: Alphastep 250 profilometer and VASE ellipsometer.

The thickness of the metal can't be measured using optical methods due to its nontransparency; so, contact profilometry was employed to measure the thickness of sputtered metal. An Alphastep 250 profilometer has a needle that can be physically dragged across the sample surface to measure the height differences thereby giving the thickness of the film deposited. The schematic graph of Alphastep 250 profilometer working process is shown in Figure 3.9.

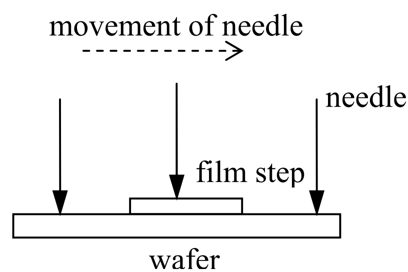

Figure 3.9 Alphastep 250 profilometer working schematics

Before deposition, a zig-zag patten was drawn on a cleaned glass wafer using a marker. After deposition, the pattern was removed using isopropyl alcohol to give a clear film step. When the needle went across the film step, the difference of

height was considered to be the film thickness. The deposition rate of metal can be determined by the film thickness and deposition time.

For oxide deposition, the thickness and deposition rate can be monitored by the quartz crystal placed under the wafer holder. An optical method is also used for verification and acquirement of optical constants such as refractive index. Use of a Variable Angle Spectroscopic Ellipsometer (VASE) was adopted to this end.

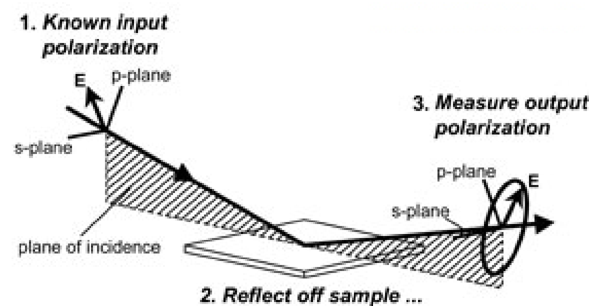

Figure 3.10 Ellipsometer working process [37]

Ellipsometry is an optical technique used for thickness measurement, optical property analysis and metrology. The ellipsometer has a polarizer which polarizes the incident light and a rotating analyzer which measures the output of the polarization. By comparing the changes of known polarized incidence and the output polarization, the ellipsometer can determine film thickness and refractive index (see Figure 3.10) [37]. A standard SiO_2 sample was used for calibration before measuring our own samples. Then our samples were measured at angles of 60°, 65° and 70°. The wavelength ranged from 300 nm to 1700 nm.

3.6.2 Resistivity measurement

For deposition of the oxide by E-beam evaporation, the NanoFab has a well-developed recipe and not many parameters can be adjusted. The bulk density, Z-factor, tooling rate are all preset; but for metal sputtering many factors such as deposition pressure, can affect the quality of the films deposited. The effects of deposition pressure on the quality of films characterized by resistivity have been investigated by John. A. Thornton [38]. Thin films have much higher resistivity than bulk materials; low resistivity often indicates high quality films meaning fewer defects, pinholes and impurities and more film uniformity.

In order to find out the relationship between sputtering pressure and film quality, metals were deposited using the BOB sputtering system under different chamber pressures. The resistivity of the films was then measured by a four point probe. The testing apparatus working schematics are shown in Figure 3.11.

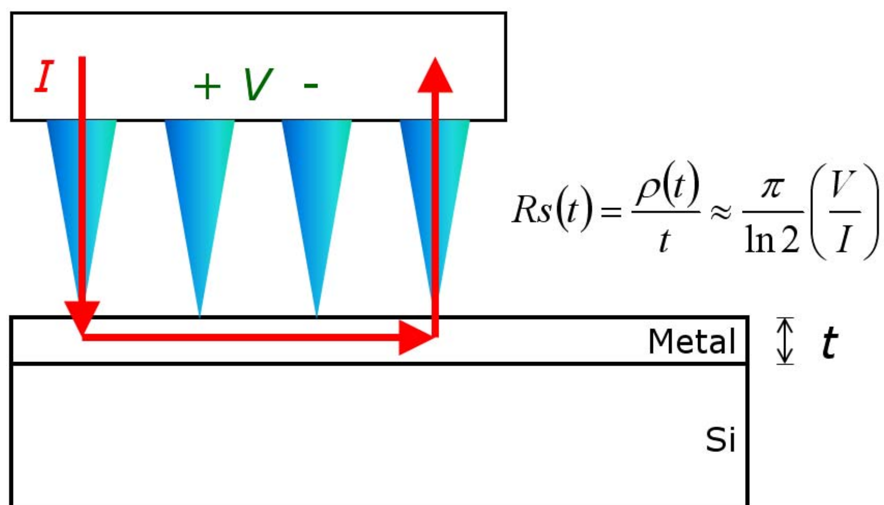

Figure 3.11 Working process of a four point probe [39]

The current is supplied by the two outer probes and goes through the metal, while voltage is measured by the two inner probes. Resistance is measured by using the four point probe. The sheet resistance can be calculated by using the formula in Figure 3.11, where Rs is the sheet resistance, t is film thickness and ρ is the resistivity.

3.6.3 Electrical performance measurement

The I-V curve of MIM junction was measured by the system shown in Figure 3.12. The measurement was done at Scanimetrics Co. Ltd. The testing system contains of a Xantrex XDL 35-5TP DC Power supply, a Keithley 196 system, a probe station with two probes and LABVIEW software program. The power supply was a source meter that can provide DC power and record voltage and current. Its resolution, however, is only 1mA; therefore, we used the Keithley 196 model to measure the current. It can measure current as low as 1 pA, which is suitable for MIM leakage current at bias voltage less than 0.5 V. LABVIEW is a software program that can be used to control the measurement parameters such as current limit, waiting time and voltage steps and record the current automatically. When testing the device, one probe was put on the top electrode covered with Au while the other one was used to scratch the SiO_2 and native Ta_2O_5 dielectric layer and contact the bottom electrode. This should be carefully done to prevent the first probe from penetrating the thin layers and causing circuit short.

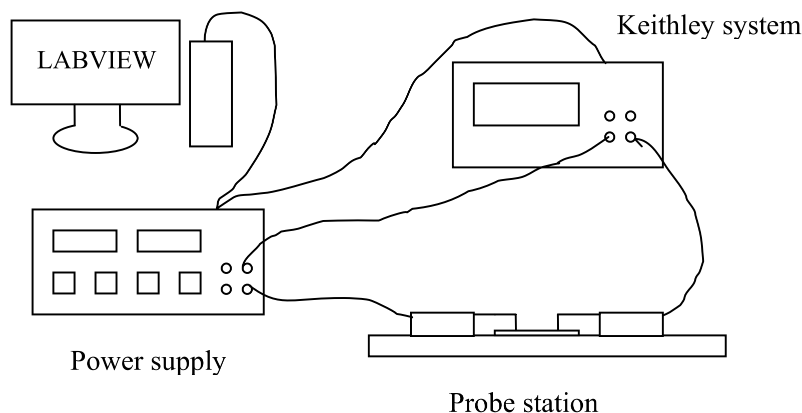

Figure 3.12 Schematic graph of measurement set-up system

The MIM devices with different thicknesses of SiO_2 layers were tested at both forward and reverse bias voltage ranging from 0 to 2 V respectively at 10 mV per step. The waiting time was set at 1000 s to give the program enough time to record a relatively steady result. The current limit was set at 1 A. The probe contacting the top electrode was kept at 45° to the sample surface in order to prevent it from penetrating the oxide layer. The other one was used to scratch the oxide layer to make a good contact with the bottom electrode. The probe contacting the bottom electrode was put in place first since it needs to penetrate the oxide layer and contact steadily with the bottom electrode. The one contacting the top electrode was lowered down very slowly until it just contacts the gold layer and a small amount of current was shown on the meter display. The voltage then was increased from 0 V to 2 V and current was recorded automatically. The current of reverse bias voltage was measured and recorded in the same way. The photo of the measurement set-up is shown in Figure 3.13.

Figure 3.13 Photo of measurement set-up

Since the measurement set-up mentioned above had a problem with auto ranging, a Keithley 4200-SCS semiconductor characterization system combined with a Suss EP 4 four-point probe station were also employed to measure the I-V and C-V characteristics of the MIM device. The photograph of the semiconductor analyzer and the probe station is shown in Figure 3.14. These pieces of equipment are located in ECERF building, University Of Alberta.

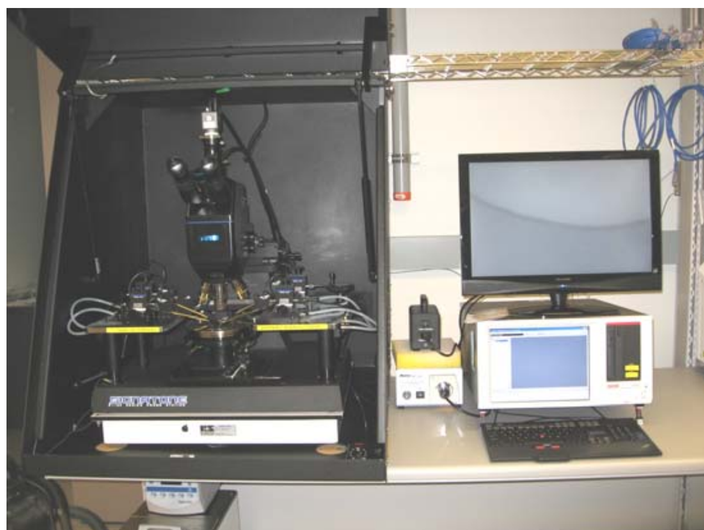

Figure 3.14 Keithley 4200-SCS model and four-probe station

The block diagram of the basic test setup is shown in Figure 3.15. The C-V measurement was carried out at AC frequencies and the capacitance C of the device under test was calculated using the equation below:

$$C = \frac{I}{2\pi f V_{AC}} \quad [40]$$

where C is the capacitance, I is the magnitude of the AC current through the device, f is the AC frequency and V_{AC} is the magnitude and phase angle of the measured AC voltage. Therefore, AC impedance is measured by applying an AC voltage and measuring the resulting AC current, AC voltage and the impedance phase angle between them.

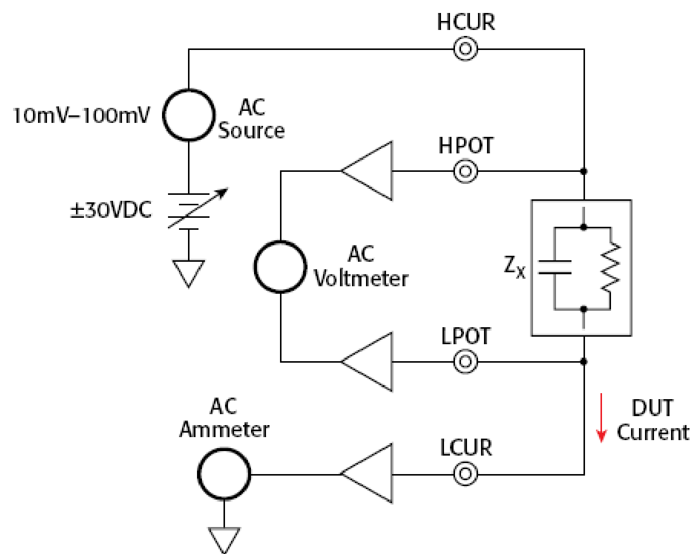

Figure 3.15 Basic test setup for C-V measurement [40]

The meter's program uses different models that take into account both series and parallel resistance associated with capacitance. The variables that can be derived from the measurement and the corresponding equations are shown in Figure 3.16.

In this study, the C-V measurement was made by sweeping the voltage from -0.5 V to 0.5 V at a frequency of 10 kHz with increments of 0.01 V. The AC voltage is 30 mV. The result gives the impedance, phase angle θ and Cp-Gp or Cs-Rs depending which model is chosen.

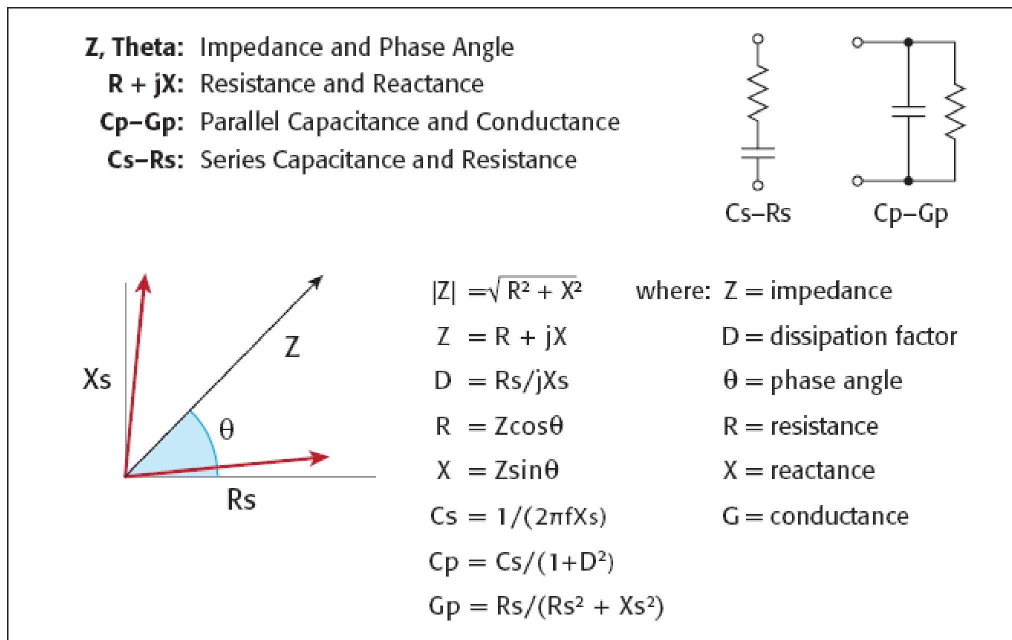

Figure 3.16 Relationship of variables derived from the measurement [40]

CHAPTER 4: RESULTS AND DISCUSSIONS

4.1 Material selection

4.1.1 Metal and oxide properties

For the MIM device to function properly, it's very important to choose the right materials for both the oxide and metal. Many factors should be considered as to select the oxide such as band gap, work function and dielectric constant. Table 4.1 shows some properties of the oxides considered.

Table 4.1 Properties of oxides

Oxide	Lattice constant(Å)	Band gap (eV)	Dielectric constant	Work function (eV)	Ref.
ZrO_2	5.07	5.8	12.5	3.12	41-43
Cr_2O_3	4.95	3.36	9.2	N/A	41, 43-44
Al_2O_3	4.785	8.8	10.5-12	4.7	41, 43-45
MgO	4.211	7.7	9.65	3.1--4.4	41-44
NiO	4.17	4.2	11.9	5.55	41-44
CoO	4.27	4	12.9	N/A	41-44
MnO	4.44	3.6	13.8	N/A	41-44
CdO	4.7	2.1	17.2	N/A	41, 43-44
TaO_2	4.709	4.2	N/A	4.65	41, 44
TiO_2	4.593	3--3.4	40--80	3.87--6.21	41-44
Nb_2O_5	6.17	3.9	N/A	N/A	41, 43-44
Ta_2O_5	6.18	4.2	~15	N/A	41, 42-45
SiO_2	4.913	9	3.9	5	41, 45

Since an electron beam evaporation system is available and SiO_2 and Al_2O_3 are the only oxides available for the system in the Nanofab, these two oxides were considered for the MIM device. With a band gap as high as 9 eV and a low dielectric constant of about 3.9, SiO_2 is a promising insulator to be sandwiched between two metals. As well, few studies have been done to investigate MIM structures with SiO_2 as the dielectric layer. Therefore, SiO2 was selected to be the insulator in the MIM device.

In studying MIM devices, a variety of combinations of materials, such as Ni-NiO-Ni (or Cr) [1,46-47], Al-Al_2O_3-Ag (or Al)[4,48] and $CoSi_2$-CaF_2- $CoSi_2$[11] have been used. S. Krishnan et al. [1] stated that MIM devices with different electrodes yield sufficient non-linearity and asymmetry, which allows significant current flow without external bias. Dissimilar metals, therefore, were originally decided upon for usage in the MIM device. Table 4.2 shows the electronic properties of the metals considered. All the metals listed have similar work functions in the range of 4~5 eV. Since large differences between the work functions of the two metals produces significant asymmetry and non-linearity, Al and Cr were originally chosen to be electrodes for the MIM device. However, the problem with the MIM junction which has SiO_2 sandwiched between Al and Cr is that it's easily shorted out when measuring its electric properties such as current-voltage characteristic. So more experiments were done on the selection of the proper materials and Ta was eventually chosen for both electrodes. Au was coated on the top electrode to prevent it from being oxidized when exposed to air.

Table 4.2 Properties of metals

Metal	Lattice constant(Å)	Work function(eV)	Electron affinity(eV)	Resistivity (μΩ-cm)	Ref.
Au	4.07	5.47	2.309	2.35	41,42,45
Ag	4.08	4.64	1.302	1.59	41,42,45
Pt	3.92	5.64	2.128	10.6	41-42
Al	4.05	4.08	0.433	2.65	41,42,45
Cu	3.615	N/A	1.235	1.67	41,42,45
Ni	3.52	5.22	1.156	7.98	41,42,49
Zr	3.62	4.05	0.426	42.9	41,42,45
Nb	3.3	4.02	0.893	12.5	41,42,45
Ta	3.306	4.25	0.322	12.45	41,42,45
Fe	2.87	4.67	0.151	9.71	41,42,45
Cr	2.88	4.5	0.666	12.9	41,42,45
W	3.165	4.55	0.815	5.65	41,42,45
Ti	2.95	~4	N/A	42	41, 45

4.1.2 Selection of electrodes

In order to get a quick feedback, a simple MIM structure was built. The schematic diagram of the structure is shown in Figure 4.1. An Al film 200nm thick was deposited on a Si(100) substrate as a strong base for the MIM structure using E-Beam Evaporation. Without breaking the vacuum, a layer of 5 nm of SiO_2 was then deposited on top of Al. The oxide layer can also protect Al from being oxidized when exposed to air. When sputtering Cr on top of SiO_2, a mask was used to create dots 5 mm in diameter as one of the electrodes. A thin layer of Au

was then sputtered without taking the sample out of the chamber to protect Cr from oxidation and to also improve the contact with the probe.

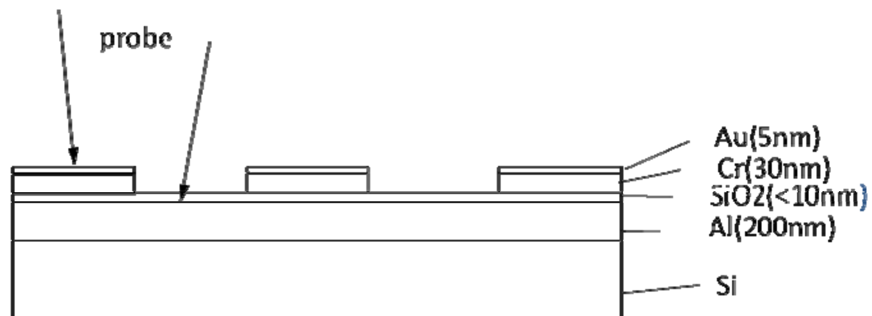

Figure 4.1 Schematic picture of Al-SiO_2-Cr/Au MIM structure

When testing the electronic properties of the structure, one probe was put on Au electrode and the other one was used to scratch the oxide layer to touch the Al electrode. The I-V curve then was recorded automatically by the software. The I-V curve of Al-SiO_2-Cr is shown in Figure4.2.

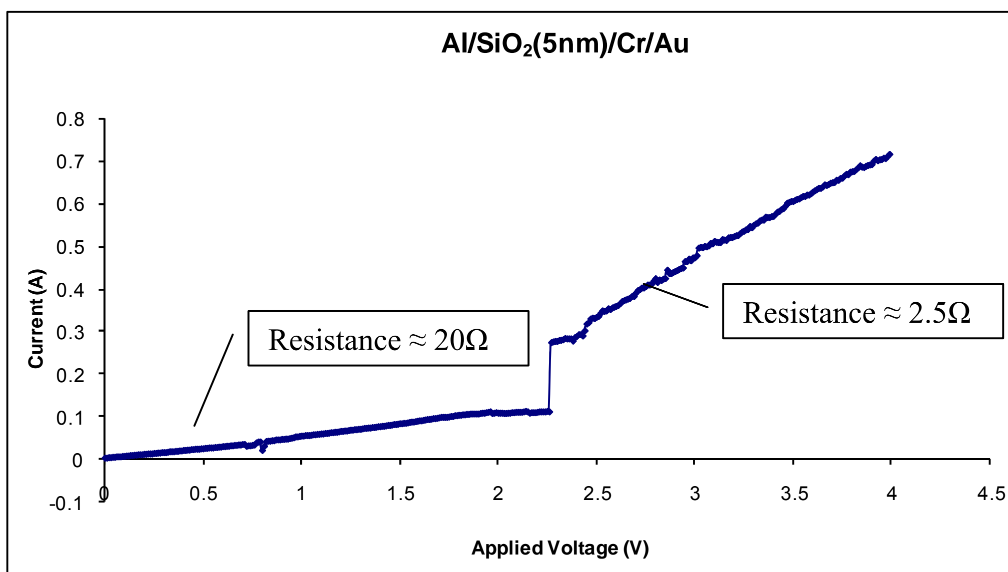

Figure 4.2 I-V curve of Al-SiO_2-Cr MIM structure

As shown in Figure 4.2, the resistance kept at a consistent level of 20 Ω until the applied voltage reached 2.3 V, and decreased to 2.5 Ω thereafter. The sudden change in the resistance indicated a possible breakdown of the device. The total resistance consisted of essential resistance, contact resistance and sample resistance before its breakdown as shown in Figure 4.3. After its breakdown, the sample resistance becomes negligible and the circuit becomes the same as when it's shorted (shown in Figure 4.3). A measurement for the shorted device (both probes touchng the Al layer) was, therefore, carried out for comparison. The result is shown in Figure4.4.

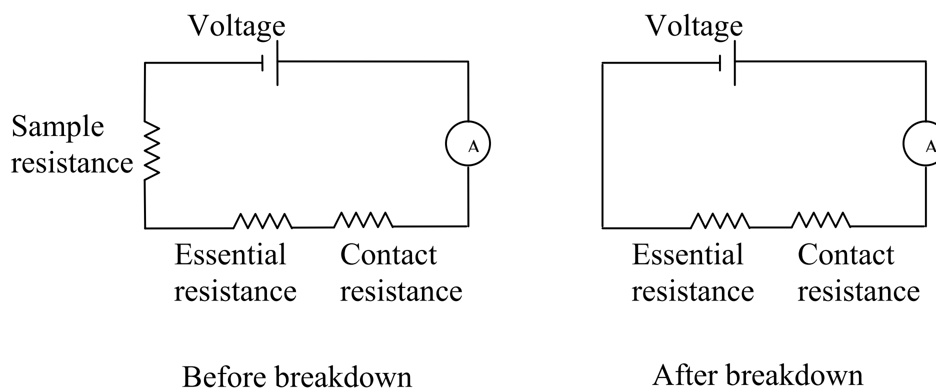

Figure 4.3 Schematic figure of resistance before and after breakdown

From the comparison, resistances for the shorted measurement and the MIM device were of the same magnitude (2.5 Ω and 1.7 Ω), which means that the MIM device either broke down or was shorted. For the MIM structure, the resistance should be around 1000 Ω instead of 20 Ω as measured because of the existence of the insulating layer. There is a high possibility, therefore, that the MIM device

was shorted before breaking down. Many factors contribute to the shorting of the MIM device such as diffusion of the metal electrode into the insulating layer, pin holes and other defects in the insulating layer. The quality of oxide layer and the interface between oxide and metal are, therefore, of great importance for the MIM device to have tunnelling current.

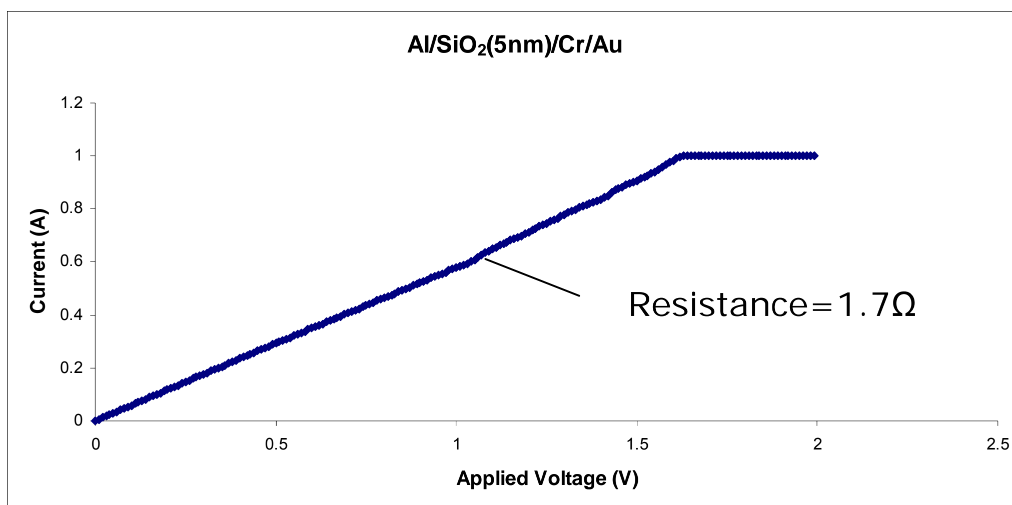

Figure 4.4 Resistance for shorted MIM device

In order to solve the shorting problem, an optimized metal-oxide combination was needed. To this end, a more simple method was adopted to test if the device was shorted or not. Different metals were deposited on Si wafers using sputtering followed by depositions of SiO_2 of the same thickness on top of the metal. Then ohm meter probes were put directly on top of the oxide layer to measure the resistance. A Four Point Probe was also used to measure the sheet resistance of the film. Most of the metals available in the NanoFab were tried to this end and the results are shown in Table 4.3.

Table 4.3 Resistance measured by Ohm-meter and Four Point Probe

Structure	Resistance	
	Ohm Meter	Four Point Probe
SiO_2/Al	1 Ω	0.056Ω
SiO_2/Cu	1.3 Ω	0.098 Ω
SiO_2/Au	1.2 Ω	0.102 Ω
SiO_2/Cr	2 Ω	0.059 Ω
SiO_2/Ta	~M Ω	~k Ω
SiO_2/Ni	~M Ω	~k Ω
SiO_2/Ti	~M Ω	~k Ω

It is evident from Table 4.3 that structures with SiO_2 on top of Al, Cu, Au, Cr were shorted when the probes were put on the oxide surface. Only structures with Ta, Ni and Ti had ~M Ω resistance and so acted as an insulator. However, Ti can easily react with SiO_2, therefore, only Ta and Ni were considered as electrodes for the MIM device.

4.1.3 Tantalum as the electrodes

To study the optical characteristics of the Ta/SiO_2/Ta/Si MIM device, every step of the deposition was studied. Three samples were needed for optical study under an ellipsometer. A silicon wafer was cut into 3 pieces, two of which were coated by 100nm of Ta. Then SiO_2 was deposited on one of the Ta/Si structures and the third piece of silicon wafer. These are shown schematically in Figure 4.5 as samples a, b and c. The samples were scanned by the ellipsometer using wavelengths from 300nm to 1700nm. Both optical properties and thicknesses

were measured for all 3 samples. The results show that the refractive index, n, of sample a is 1.51, sample b 2~5 and sample c 1.51. The refractive index of measured films and corresponding bulk materials are compared in Table 4.4.

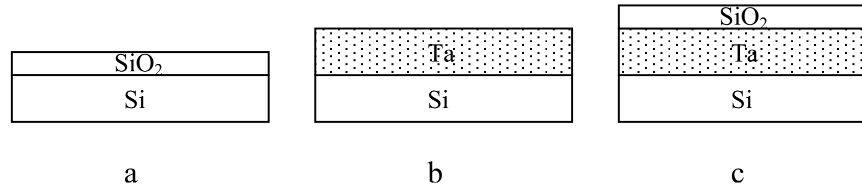

Figure 4.5 Structures of 3 samples for optical testing

Table 4.4 Comparison of refractive index for deposited films and bulk materials

Sample	Refractive index n (measured)	Bulk material	Refractive index n (bulk)
a	1.5~1.55	SiO_2 α-crystalline	1.52~1.58 [50]
b	2~5	Ta	<1 [51]
c	1.5~1.55	SiO_2 α-crystalline	1.52~1.58 [50]

The refractive index of SiO_2 (α-crystalline) is ranged from 1.52 to 1.58 at 300nm to 1700nm wavelength, which was similar to that of samples a and c. However, there was a big difference between sample b and bulk Ta. Since Ta is a metal, its refractive index should be less than 1, but the tested film showed a refractive index of 2~5. Ta_2O_5 has a refractive index of 2.1 [52], which is similar to the tested result. This means that the Ta was oxidized when exposed to air. So the device was modified to a MIIM structure which is shown in Figure 4.6.

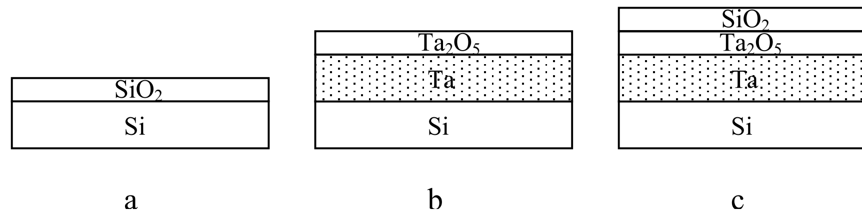

Figure 4.6 The actual structure of deposited samples

The thickness of SiO_2 in sample a and c were shown in Table 4.5. Since the Si wafer has native oxide of about 2 nm, measured independently, the thickness of the deposited SiO_2 in sample a and c are the same.

Table 4.5 Thickness of SiO_2 in sample a and c

Sample	Thickness of SiO_2 (nm)	Mean Square Error (MSE)
a	13.373±0.0211	1.904
c	10.981±0.0287	2.177

4.2 Effects of sputtering pressure on Ta resistivity

In order to find the optimized sputtering pressure for the electrode, Ta was sputtered at 2, 4, 6, 7 and 9 mTorr and resistivity was then measured using a Four Point Probe. The results are shown in Figure 4.7. The film sputtered at 6 mTorr yields the lowest resistivity which is closest to the bulk resistivity. Therefore the 6 mTorr was selected as the sputtering pressure for Ta to get a high quality film. At 6 mTorr, the deposition rate achieved was 8 nm/min.

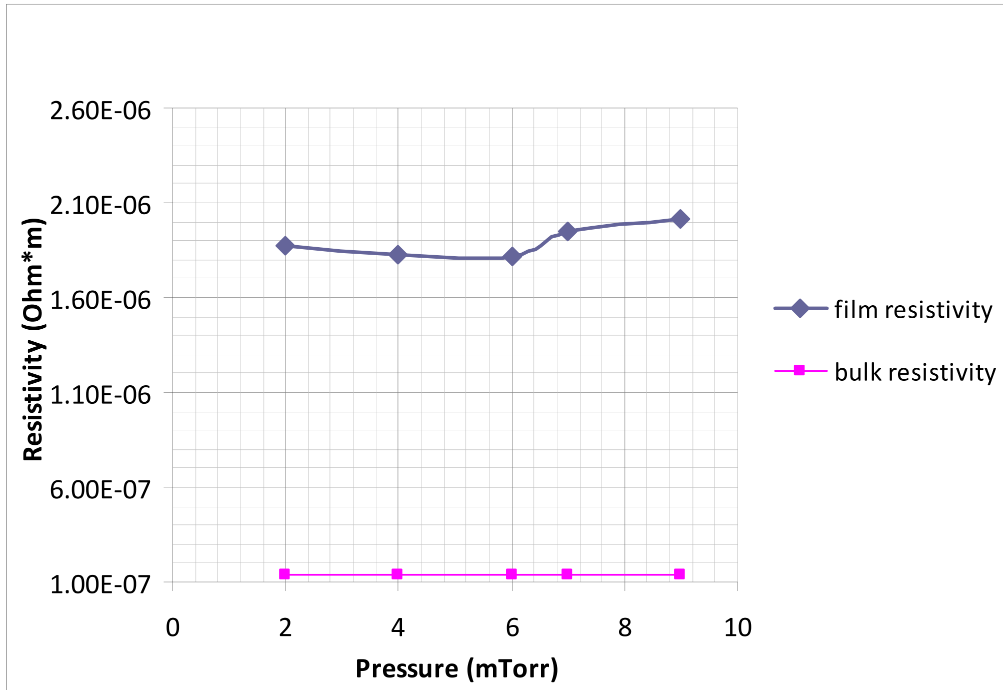

Figure 4.7 Effects of sputtering pressure on Ta resistivity

4.3 Current –voltage characteristics

An I-V curve is important for evaluation of the MIM device performance as mentioned in earlier sections. In order to investigate the I-V characteristic of the fabricated devices, MIM samples with SiO_2 thicknesses of 2, 5 and 8nm were prepared. The oxide layer thicknesses were monitored by the crystal quartz on E-beam evaporator. These samples were tested using the setup mentioned in 3.6.3. For the forward bias, voltage was set to automatically increase from 0 to 2 V in 10 mV steps. The Keithley 196 multimeter measured the current which was recorded automatically by the LABVIEW software and stored computer as x.dat files. For the reverse bias, voltage was swept from 0 to -2 V in 10 mV steps automatically and the data was measured and stored in the same way. The data was then plotted

in different ranges in order to show the behaviour clearly. For the -0.3 V to 0.3 V range, the current value was shown every 10 mV. While for other ranges, values were picked every 100 mV to show the trend of the I-V curve. Figure 4.8 shows the I-V curve of MIM device with 2 nm of SiO_2 as the insulating layer. In Figure

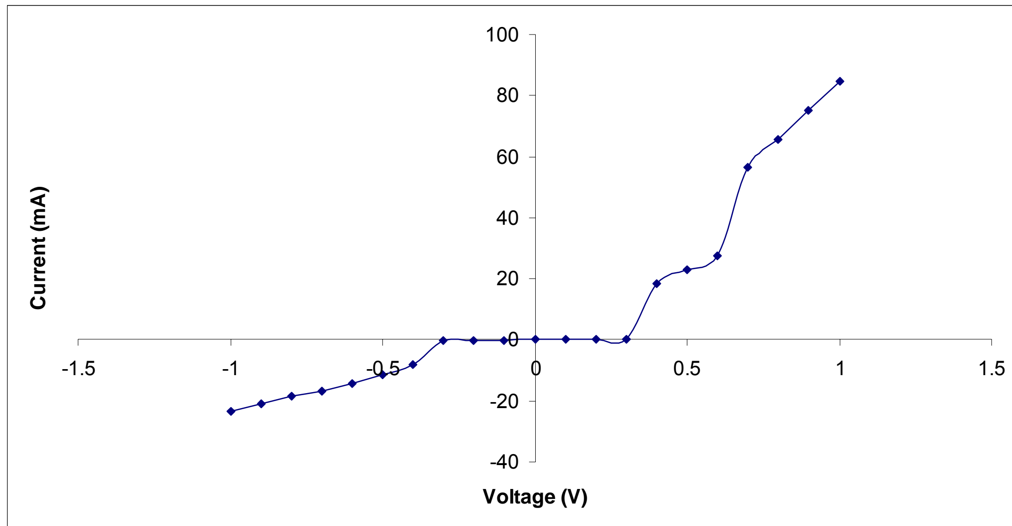

(a)

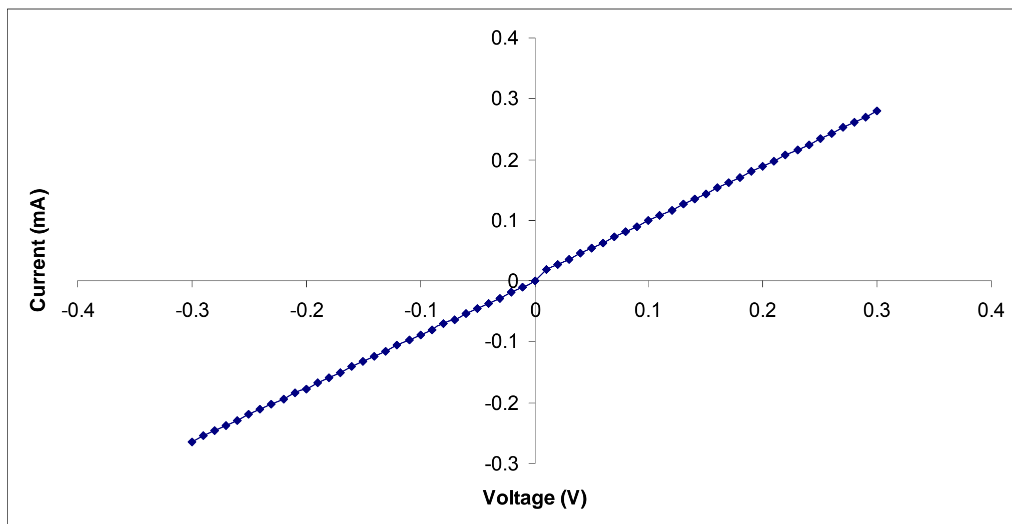

(b)

Figure 4.8 I-V curves of MIM devices with 2 nm of SiO_2 within different voltage ranges

4.8(a), the I-V curve was plotted within -1 V to 1 V. For bias voltage from -0.3 V to 0.3 V, the currents are quite small and close to 0. From 0.3 V to 0.7 V, current increase significantly and nonlinearly with the bias voltage. For voltage above 0.7 V, the current increased with bias smoothly. The little drops in current below 1 mA on the positive x axis were due to the graph drawing system not due to the current decreasing below zero suddenly. The I-V curve for -0.3 V to 0.3 V is shown in Figure 4.8(b). From this graph, current increased proportionally with bias voltage indicating linearity. Current was measured to be 0.3 mA at 0.3 V, which gave a resistivity of 1 kΩ demonstrating a very low leakage current. With the increase in the bias voltage, leakage current increased and shows nonlinearity on the current-voltage curve. Similar trends were observed for MIM devices SiO_2 thicknesses of with 5 nm and 8 nm. All the devices, regardless of the insulator thickness, demonstrate the same resistivity from -0.3 V to 0.3 V.

4.4 Auto ranging problem

On the I-V graphs for the samples discussed above, there were sudden increases in the current with the voltage. Those step-ups are primarily due to the auto ranging problem of the Keithley 196 system that was used for current measurement. The Keithley 196 digital multimeter has 5 ranges and resolutions as shown in Table 4.6. At around 0.3 mA, the circuit switched from the 300 μA range to the 3 mA range. When this occurred, the internal resistance of the Keithley meter changed from 1 kΩ to 100 Ω, resulting in a sudden drop in the total resistance of the whole circuit. This accounted for the sudden rise of current on the I-V curve. Since the resistance of the device under test was very small

compared to the internal resistance of the testing system within the 300 μA range, all the three samples exhibited similar I-V characteristics below 0.3 mV.

Table 4.6 Range and resolution of the Keithley 196 multimeter

Range	Resolution	Internal resistance
300 μA	1 nA	1 kΩ
3 mA	10 nA	100 Ω
30 mA	100 nA	10 Ω
300 mA	1 μA	2 Ω
3 A	10 μA	1 Ω

4.5 C-V characteristics

Since auto ranging issues happened when using the Keithley 196 multimeter, the Keithley 4200-SCS was used to test the C-V properties of the same samples. The tests were made at AC frequencies and the results are shown in Figure 4.9 and 4.10. The Cs-Rs curves shown in Figure 4.9 demonstrate how capacitance and resistance vary with voltage, considering the capacitor and resistor in series. With the voltage swept from 0.5 V to 0.5 V, the resistance varied within the range of 158 Ω to 167 Ω. With forward bias, the resistance increased a little and then dropped down quickly. A similar trend was observed with reverse bias. Since the resistance was not constant with the AC bias voltage, current flowing through the MIM device varied nonlinearly with the bias voltage. The capacitance increased from 2×10^{-7} Farads to 4.5×10^{-7} Farads with the voltage increased from 0 V to 0.5 V.

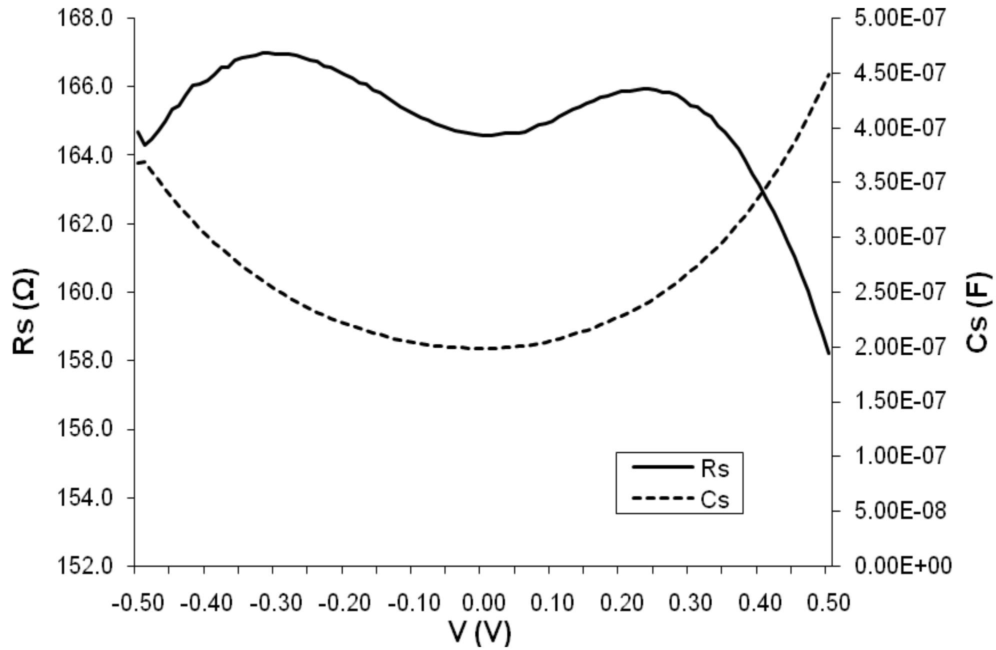

Figure 4.9 Cs-Rs of CV sweep for MIM with 8 nm of SiO_2

Figure 4.10 shows how capacitance and conductance varied with voltage, considering the capacitor and resistor in parallel. The increase in the conductance indicated the decrease in the resistance, which agreed with Figure 4.9. The capacitance decreased from 3.8×10^{-8} Farads to 2.2×10^{-8} Farads. The capacitance tested either way was quite small and the resistance changes were not large. Therefore, this device was more of a resistor than a capacitor. This can also be explained by Figure 4.11.

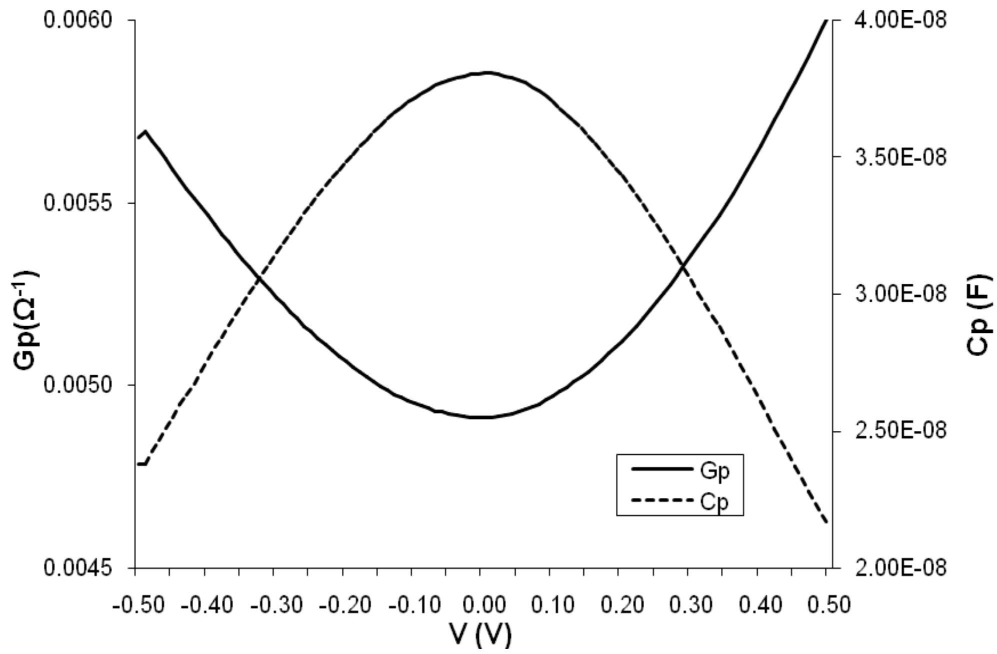

Figure 4.10 Cp-Gp of CV sweep for MIM with 8 nm of SiO_2

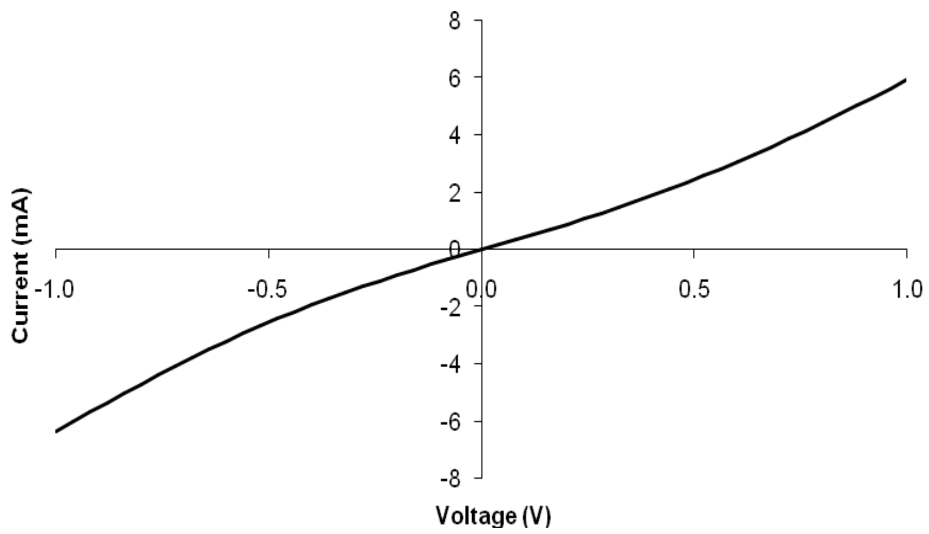

Figure 4.11 I-V curve of MIM with 8 nm SiO_2

Figure 4.11 shows the I-V curve of the MIM device with 8 nm of SiO_2 that was tested by Keithley 4200-SCS. This test was carried out with DC current. Since this analyzer did not have the auto ranging problem, the I-V curve does not show the sudden step-ups as in Figure 4.8. It is almost a straight line with some non-linearity above 0.5 V. Figure 4.12 and Figure 4.13 show the Cs-Rs and Cp-Gp curves of CV sweep for the MIM device with 5 nm of SiO_2, respectively. A similar trend was observed for the MIM with 5nm of SiO_2. When the Cs-Rs model was chosen, the resistance was reduced from 82 Ω to 76 Ω and capacitance was around 3.5×10^{-6} Farads to 6.5×10^{-6} Farads. For the Cp-Gp model, the capacitance varied from 6.5×10^{-9} Farads to 1×10^{-8} Farads. Compared to MIM with 8 nm of SiO_2, the one with 5 nm of SiO_2 possessed a higher series capacitance because capacitance is reversely proportional to the thickness of the insulator.

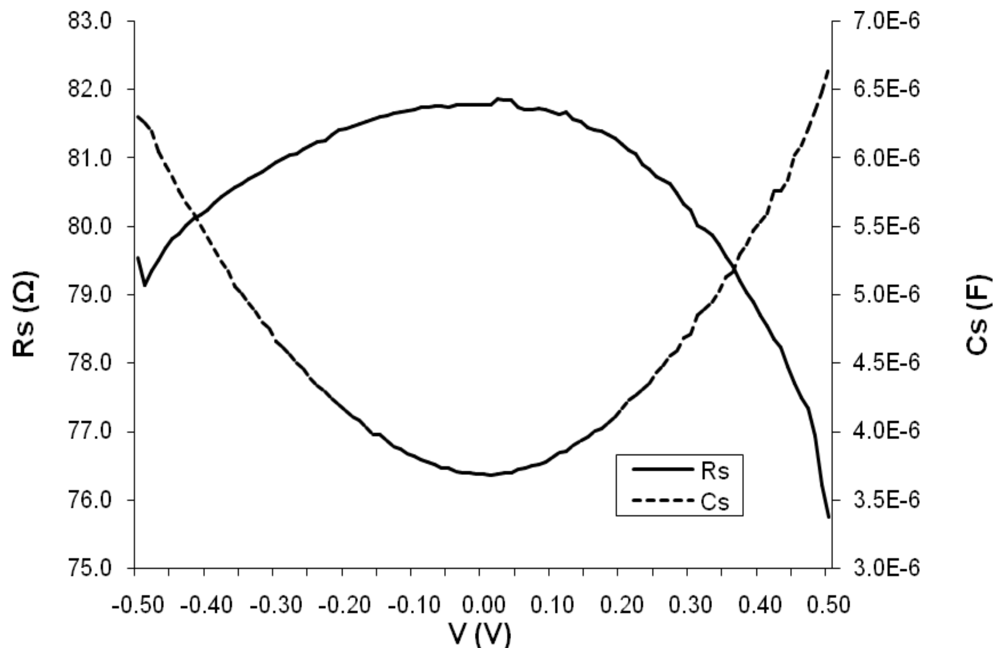

Figure 4.12 Cs-Rs of CV sweep for MIM with 5nm of SiO_2

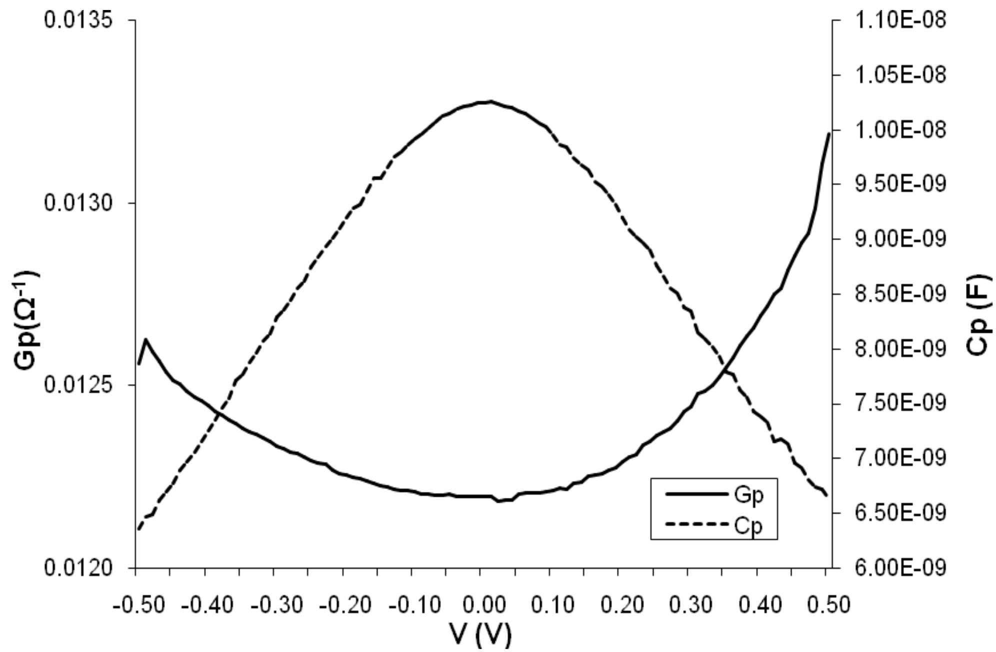

Figure 4.13 Cp-Gp of CV sweep for MIM with 5 nm of SiO_2

Since the series resistance was not constant at AC frequency, the corresponding I-V curve should not be linear. However, the I-V curve tested at DC current was almost linear, as shown in Figure 4.14. The resistance obtained at DC current is about 77 Ω, which falls into the range of the resistance derived at AC frequency.

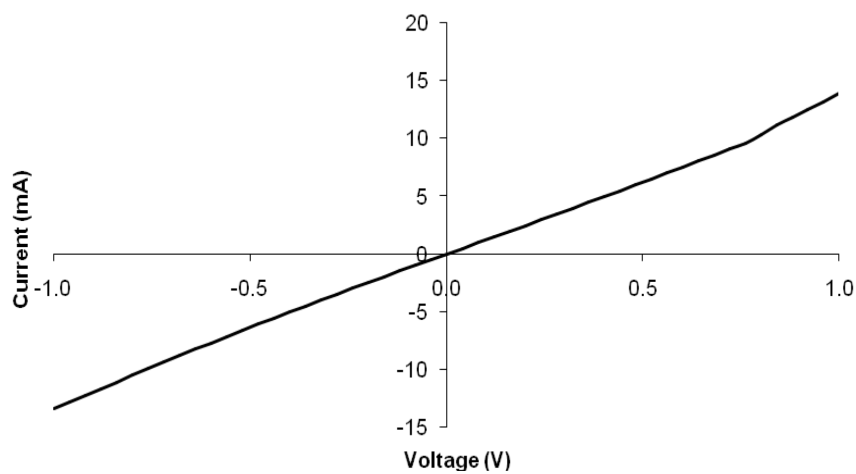

Figure 4.14 I-V curve of MIM with 5nm SiO_2

To compare the capacitance of the two samples more clearly, the voltage dependence of series capacitance is drawn in Figure 4.15. It's evident that the 5 nm SiO_2 based MIM exhibited a larger change of capacitance with voltage. On the other hand, the MIM with 8 nm of SiO_2 had a much lower and more stable capacitance in the range of ~10^{-7} Farads. In order to compare the variation of capacitance for MIM device with 5 nm and 8 nm of SiO_2, the series capacitance was normalized and plotted against voltage. Normalized capacitance is the ratio of measured capacitance (C) to zero bias capacitance (C_0). The normalized capacitances of SiO_2 MIM with different thickness are illustrated in Figure 4.16. Variation of capacitance was increased as the thickness of SiO_2 increased from 5 nm to 8 nm. It can be seen from the graph that the nonlinearity of 5 nm SiO_2 based MIM is less pronounced.

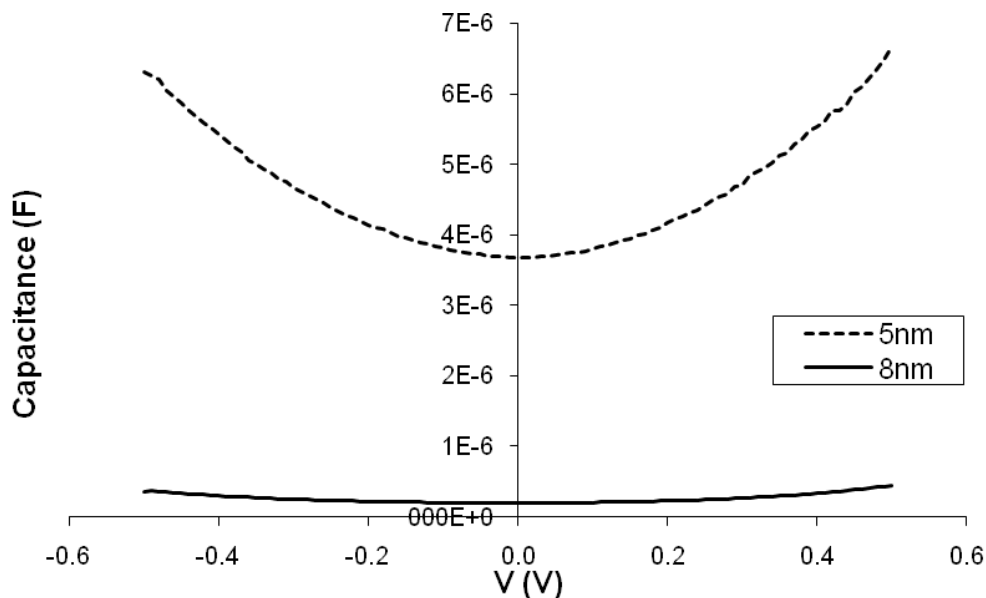

Figure 4.15 Voltage dependence of Capacitance with different thickness of SiO_2

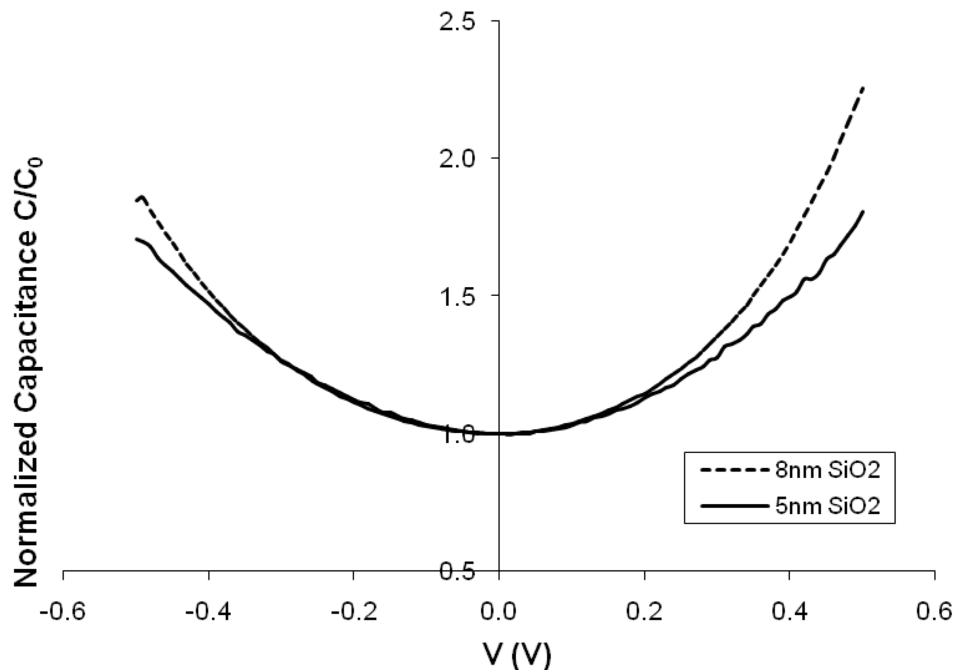

Figure 4.16 Voltage dependence of the normalized capacitance of SiO_2 MIMs

In this study, the same tests were also carried out on a MIM device with 2 nm of SiO_2. However, negative capacitance was obtained for both Rs-Cs and Cp-Gp model (see Figure 4.17 and Figure 4.18). This indicated that there was barely any insulating layer in the MIM device and a conductor was possibly achieved. Figure 4.19 shows the I-V curve for the MIM with 2 nm of SiO_2, from which a resistance of 20 Ω was derived. Its leakage current was about 10 times that of the MIM with 8 nm SiO_2.

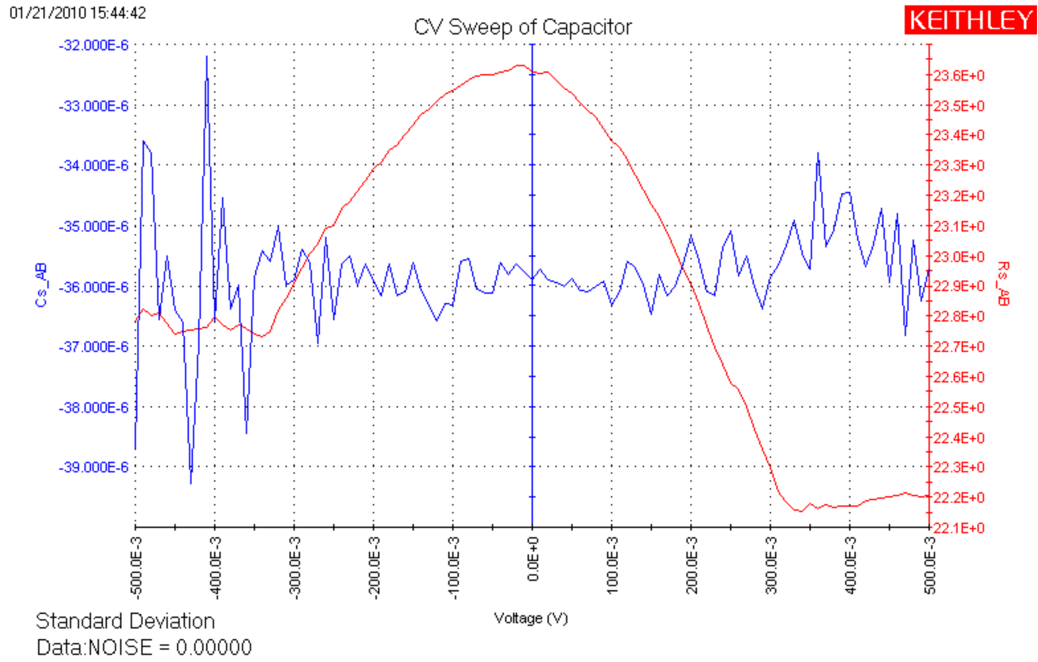

Figure 4.17 Cs-Rs of CV sweep for MIM with 2nm of SiO_2

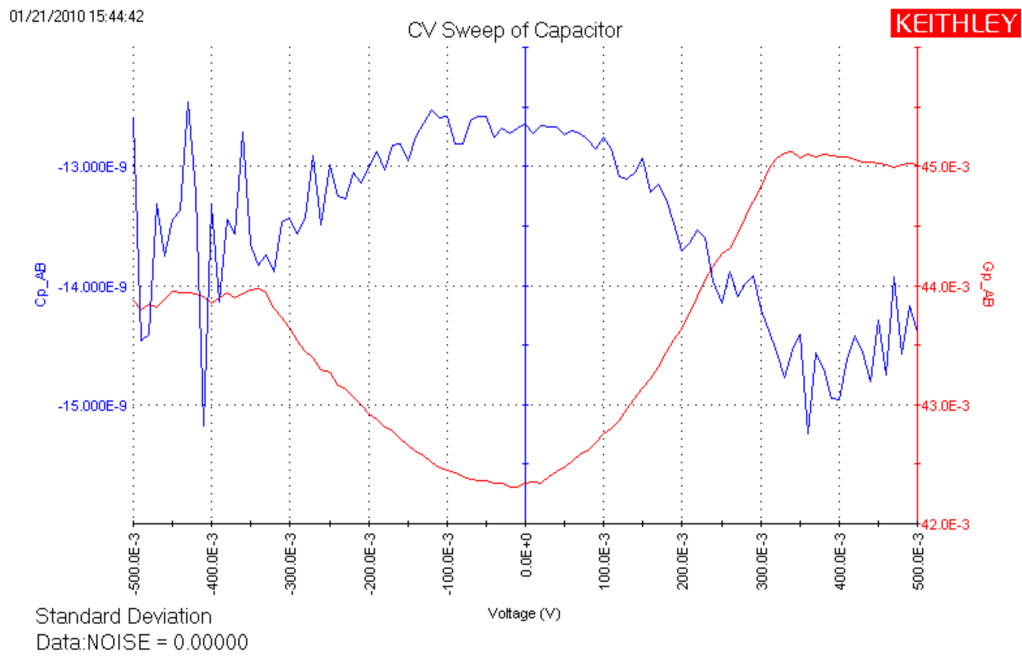

Figure 4.18 Cp-Gp of CV sweep for MIM with 2nm of SiO_2

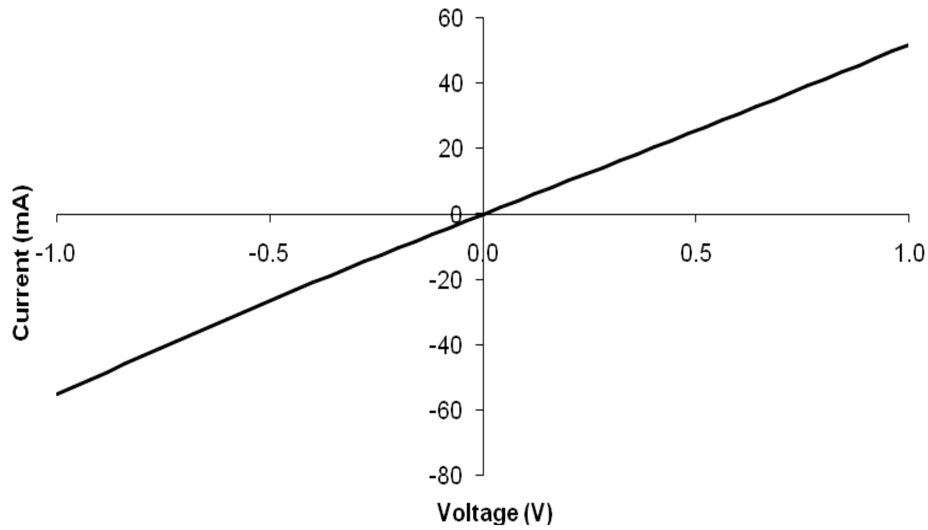

Figure 4.19 I-V curve of MIM with 2nm SiO_2

The resistance decreased with the reduction of the insulator thickness in the MIM devices. This was not hard to understand considering the thin insulator and the large contact area. As mentioned earlier, the contact area was approximately 19.6mm^2 and the thicknesses were less than 10 nm. Since E-beam evaporation is a low power process compared to sputtering, the evaporated SiO_2 molecular had lower kinetic energy. The molecules did not have enough power to move around and coalesce. The adhesion of SiO_2 deposited by E-beam to the substrate is not perfect; therefore, defects in the device were not negligible. The pin holes in the SiO_2, for example, could let the electrons go through the insulating layer without either climbing over the energy barrier or tunnelling through it. Also, with the large contact area, the possibility of the electrons traveling through the defects got higher. This will eventually enhance the features of MIM as a resistor and decrease its capacitance.

In order to understand how insulator thickness affects the leakage current, leakage current at 0.2 V bias was plotted against SiO_2 thickness, as shown in Figure 4.20.

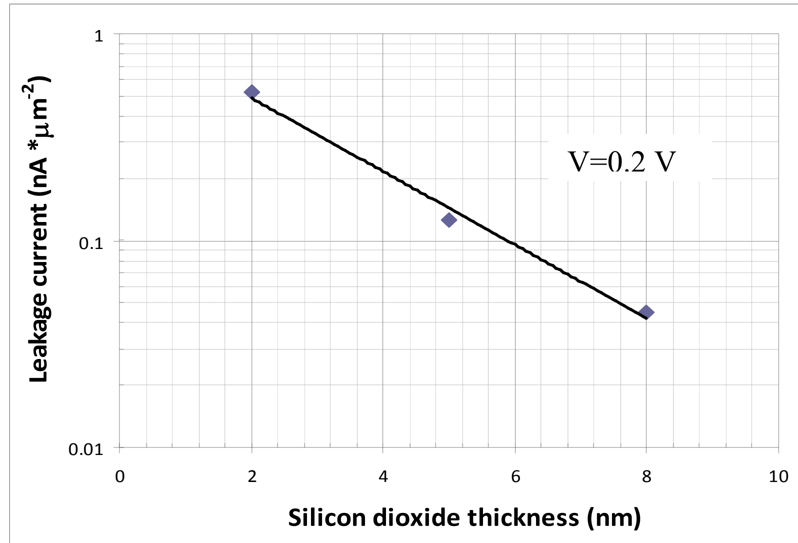

Figure 4.20 Leakage current versus SiO_2 thickness at 0.2 volts bias

It is observed from the graph that the leakage current decreased exponentially as the SiO_2 thickness increases. Among the three samples, the MIM with 8 nm of SiO_2 exhibited the lowest leakage current, which indicated the most efficient insulating layer. According to Fowler-Nordheim equation [53], the tunnelling current density is:

$$J = K_1 \cdot E^2 \exp(-\frac{K_2}{E}),$$

where

$$K_1 = \frac{m}{m^*} \frac{q^3}{8\pi h \phi_B}$$

$$K_2 = \frac{8\pi}{3} \left(2 \frac{m^*}{h^2} \right)^{1/2} \frac{\phi_B{}^{3/2}}{q}$$

and J, E, m, m^*, q, h and Φ_B are respectively the current density, electric field, electron mass, effective mass of electron in dielectrics, the electronic charge, the Plank's constant and the barrier height of the injecting electrode. The current density decreases as the electric field decreases. Since $E = \frac{V}{t}$, where V is the bias voltage and t is the dielectric thickness, the current density decreases with the thickness of insulating layer. The same trend was observed from Figure 4.20.

From the Fowler-Nordheim equation, we get $\ln \frac{J}{E^2} = \ln K_1 - \frac{K_2}{E}$. Therefore, when the Fowler-Nordheim mechanism is dominant, a plot of $\ln \frac{J}{E^2}$ vs. $\frac{1}{E}$ should be linear. At a constant bias voltage, E only varies with the thickness t. To this end, $\ln \frac{J}{E^2}$ was plotted against t in Figure 4.21.

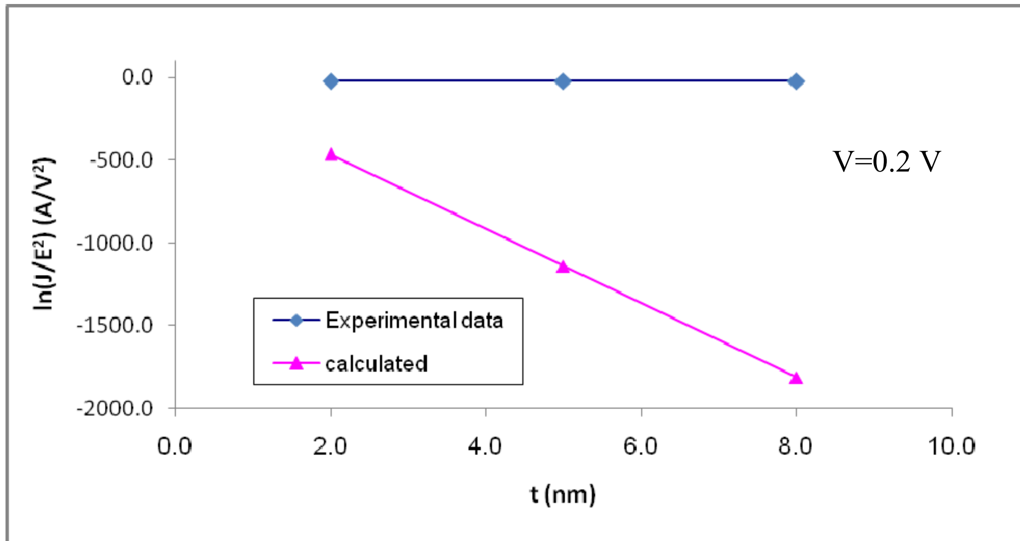

Figure 4.21 ln(J/E^2) vs. t plots for MIM with different SiO_2 thickness

Since K_1 and K_2 only depend on the electron effective mass and the barrier height of the injecting electrode, with a given effective mass and a barrier height these constants can be calculated and vice versa. The band gap of SiO_2 is 9 eV and the bias voltage is 0.2 V, the potential barrier is estimated to be 4.7 eV. A value of 0.42m was used for effective mass of electrons in SiO_2. Both K_1 and K_2 were calculated from the equations mentioned above. As a comparison, the calculated line was plotted in Figure 4.21 as well. There is a large difference between the graph based on experimental data and the calculated line. This discrepancy is probably due to the defects in the films such as pinholes and impurities, which give rise to the much larger leakage currents than predicted by tunnelling.

CHAPTER 5:   CONCLUSIONS AND FUTURE WORK

5.1 Conclusions

In this study, the E-beam evaporated SiO_2 was evaluated as the insulating layer for a Ta-SiO_2-Ta symmetric MIM. The process of material selection was carried out by depositing SiO_2 onto the different electrodes and testing the optical and electrical characteristics. The metal electrodes were deposited by DC magnetron sputtering, while the insulating layer sandwiched between was evaporated using E-beam evaporation. After the materials were selected, the MIM device was then fabricated on the Si substrate by using a shadow mask. Originally, the I-V characteristics of MIM structures with 2 nm, 5 nm and 8 nm of SiO_2 were measured using Keithley 196 digital multimeter. The Keithley 196 meter had an auto ranging problem, therefore, step-ups in the I-V curves which primarily contributed to the nonlinearity were due to change of the internal resistance of the measuring system. In order to solve this problem, C-V measurements were carried out using a Keithley 4200-SCS system combined with a four probe station. C-V measurements were made at AC frequencies by sweeping voltage from -0.5 V to 0.5 V. I-V tests were also implemented using this system at DC current. The results show little nonlinearity in the I-V curve. However, the C-V dot measurements showed a resistance and capacitance varying with bias voltage. As thickness of the insulting layer was reduced, the resistance of the MIM device decreased accordingly, indicating the existence of defects in the SiO_2 layer. The MIM with 8 nm of SiO_2 had a much lower and more stable capacitance in the

range of ~10^{-7} Farads. The MIM device with 2 nm of SiO_2, however, exhibited a negative capacitance which meant there was no effective insulating layer sandwiched between the metals. According to this study, E-beam evaporated SiO_2 is not desirable for use in MIM devices for several reasons. Since E-beam evaporation is a low power deposition, the quality of SiO_2 layer was inferior. Also, the small insulator thickness and the large contact area allow more current flow through the defects, making the MIM device act like a resistor.

5.2 Future work

In the material selection section, Ni and Ta are both selected as the potential electrodes that might work in the MIM device. This study is only focused on Ta as the electrodes. So in the future work, Ni can be taken as the electrodes and a Ni-SiO_2-Ni MIM device can be fabricated and measured. In this study, the device is fabricated using a shadow mask, which gives a contact area of about 19.6 mm^2. In the future work, photolithography can be employed to fabricate the device so that the contact area can be reduced significantly. In addition, SiO_2 can be deposited using Atomic Layer Deposition (ALD) to increase its quality. The barrier height of the MIM structure can also be calculated after a nonlinear I-V curve is achieved.

REFERENCES

[1] S. Krishnan, E. Stefanakos and S. Bhansali, "Effects of dielectric and contact area on current-voltage characteristics of thin film metal-insulator-metal diodes," Thin Solid Films, Vol. 516, pp. 2244-2250, 2008.

[2] S. Hong, C. Lee, J. Han and W. Kim et al, "Flexible metal-insulator-metal (MIM) devices for plastic film AM-LCD," Current Applied Physics, Vol. 2, pp. 245-248, 2002.

[3] M. R. Abdel-Rahman, F. J. Gonzalez and G. D. Boreman, "Antenna-coupled metal-oxide-metal for dual band detection at 92.5 GHz and 28THz," Electronics Letters, Vol. 40, No. 2, pp. 116-118, 2004.

[4] G. M. Elchinger, A. Sanchez, C. F. Davis, Jr., and A. Javan, "Mechanism of detection of radiation in a high-speed metal-metal oxide-metal junction in the visible region and at longer wavelengths," J. Appl. Phys., Vol. 47, No. 2, pp. 591-594, 1976.

[5] Phiar Corporation, "A new technology for terahertz electronics," A whitepaper for Phiar Corporation, 2003

[6] L. Esaki, "New phenomenon in narrow germanium p-n junctions," Phys. Rev. Vol. 109, pp. 603, 1958.

[7] S. M. Sze and K. K. Ng, Physics of semiconductor devices 3rd ed., Wiley, New Jersey, pp. 420, 1981.

[8] R. Tsu and L. Esaki, "Tunneling in a finite superlattice," Appl. Phys. Lett. Vol. 22, pp. 562, 1973.

[9] H. Mizuta and T. Tanoue, "The physics and applications of resonant tunneling diodes," pp. 10, 2006.

[10] D. A. Neamen, Semiconductor physics and devices: basic principles 3rd ed., McGraw-Hill, Boston, 2003.

[11] T. Suemasu, M. Watanabe, J. Suzuki and Y. Kohno, "Metal($CoSi_2$)/insulator(CaF_2) resonant tunneling diode," Jpn. J. Appl. Phys. Vol. 33, pp. 57-65, 1994.

[12] K. Maezawa, "A new generation of negative-resistance-devices—New developments in ultrahigh-frequency applications based on resonant tunneling elements," Electronics and Communications in Japan, Part 2, Vol. 89, No. 4, pp. 29-37, 2006.

[13] J. C. Fisher and I. Giaever, “Tunneling through thin insulating layers” J. Appl. Phys. Vol. 32, pp. 172, 1961.

[14] P. Esfandiari, G. Bernstein, P. Fay, W. Porod, B. R. Zarandy, B. Berland, L. Boloni, G. Boreman, B. Lail, B. Monacelli and A. Weeks, “ Tunable antenna-coupled metal-oxide-metal(MOM) uncooled IR detector,” Proc. of SPIE, Vol. 5783, pp. 470-482, 2005.

[15] J. Frenkel, “Electrical resistance of contacts between solid conductors,” J. Phys. Rev. Vol. 36, pp. 1604, 1930.

[16] R. Stratton, “Volt-current characteristics for tunneling through insulating films,” J. Phys. Chem. Solids, Vol. 23, pp. 1177-1190, 1962.

[17] J. G. Simmons, “Generalized formula for the electric tunnel effect between similar electrodes separated by a thin insulating film,” J. Appl. Phys. Vol. 34, No.6, 1963.

[18] S. Krishnan, “Design, fabrication and characterization of thin-film M-I-M diodes for rectenna array,” Master Thesis of University of South Florida, 2004.

[19] B. Berland, “Photovotaic technologies beyond the horizon: optical rectenna solar cell,” NREL Subcontractor Final Report, ITN Energy Systems, Inc., 2003.

[20] K. H. Gundlach and J. Holzl, “Logarithmic conductivity of Al-Al_2O_3-Al tunneling junctions produced by plasma and by thermal oxidation,” Surface Science, Vol. 27, pp. 125-141, 1971.

[21] J. G. Simmons, “Potential barriers and emission-limited current flow between closely spaced parallel metal electrodes,” J. Appl. Phys. Vol. 35, pp. 2472, 1964.

[22] E. Wiesendanger and F. K. Kneubuhl, “Thin-film MOM-diodes for infrared detection,” J. Appl. Phys. Vol. 13, pp. 343, 1977.

[23] K. M. Evenson, M. Inguscio and D. A. Jennings, “Point contact diode at laser frequencies” J. Appl. Phys. Vol. 57, pp. 956, 1985.

[24] J. W. Dees, “Detection and harmonic generation in the sub-millimeter wavelength region,” J. Microw. Vol. 9, pp. 48-55, 1966.

[25] L. O. Hocker, D. R. Sokolof, V. Daneu, A. Szoke and A. Javan, “Frequency mixing in the infrared and far-infrared using a metal-to-metal point contact diode,” Appl. Phys. Lett. Vol. 12, pp. 401, 1968.

[26] S. M. Faris, T. K. Gustafson and J. C. Wiesner “Detection of optical and infrared ... metal-barrier-metal diodes,” J. IEEE Quantum Electronics, Vol. QE-9, pp. 737, 1973.

[27] D. A. Jennings, F. R. Petersen and K. M. Evenson, “Extension of absolute frequency measurements to 148 THz: frequencies of 2.0- and 3.5 μm Xe laser,” Appl. Phys. Lett. Vol. 26, pp. 510, 1975.

[28] O. Acef, L. Hilico, M. Bahoura, F. Nez and P. De Natale, “Comparison between MIM and schottky diodes as harmonic mixers for visible lasers and microwave sources,” Optics Communications, Vol.109, pp. 428-434, 1994.

[29] T. K. Gustavson and T. J. Bridges, “Radiation of difference frequencies produced by mixing metal-barrier-metal diodes,” Appl. Phy. Lett. Vol. 25, No.1, pp. 56-59, 1974.

[30] J. G. Small, G. M. Elchinger, A. Javan, A. Sanchez, F. J. Bachner and D. L. Smythe, “AC electron tunneling at infrared frequencies: thin-film M-O-M diode structure with broad-band characteristics,” Appl. Phys. Lett. Vol. 24, pp. 275, 1974.

[31] S. Y. Wang, T. Izawa and T. K. Gustafson, “Coupling characteristics of thin-film metal-oxide-metal diodes at 10.6 μm,” Appl. Phys. Lett. Vol. 27, pp. 481, 1975.

[32] A. Sanchez, C. F. Davis Jr., K. C. Liu and A. Javan, “The MOM tunneling diode: Theoretical estimate of its performance at microwave and infrared frequencies,” J. Appl. Phys. Vol. 49, pp. 5270, 1978.

[33] I. Wilke, Y. Oppliger, W. Herrmann and F. K. Kneubuhl, “Nanometer thin-film Ni-NiO-Ni diodes for 30THz radiation,” J. Appl. Phys. Vol. A 58, pp. 329-341, 1994.

[34] B. Tiwari, J. A. Bean, G. Szakmany, G. H. Bernstein, P. Fay and W. Porod, “Controlled etching and regrowth of tunnel oxide for antenna-coupled metal-oxide-metal diodes,” J. Vac. Sci. Technol. Vol. B 27, No. 5, pp. 2153-2160, 2009.

[35] L. B. Freund, Thin film materials: stress, defect formation, and surface evolution, Cambridge University Press, New York, 2003.

[36] http://vs03013.virtualserver.priorweb.be/index.php?p=69&m=2

[37] http://www.jawoollam.com/tutorial_4.html

[38] J. A. Thornton, “The microstructure of sputter-deposited coatings,” J. Vac. Sci. Technol. Vol. 11, pp. 666-670, 1974

[39] S. Jim and K. Cadien, “Effect of deposition variables on the electrical properties of Pt thin films,” CMSC presentation, 2008.

[40] L. Stauffer, “Fundamentals of semiconductor C-V measurements,” Keithley Instruments, Inc., 2009.

[41] R. W. G. Wyckoff, Crystal structure 2nd ed., Interscience, New York, 1963.

[42] D. R. Lide, CRC hand book of chemistry and physics 90th ed., CRC, 2009.

[43] G. V. Samsonov, The oxide handbook 2nd ed., IFI/Plenum, New York, 1982.

[44] C. B. Carter and M. G. Norton, Ceramic materials, Springer, New York, 2001.

[45] A. P. Murarka, Metallization: Theory and practice for VLSI and ULSI, Butterworth-Heinemann, Oxford, 1993.

[46] P. C. D. Hobbs, R. B. Laibowitz and F. R. Libsch, “Ni-NiO-Ni tunnel junctions for terahertz and infrared detection,” Applied Optics, Vol. 44, No. 32, pp. 6813-6822, 2005.

[47] S. Krishnan, H. La Rosa, E. Stefanakos, S. Bhansali and K. Buckle, “ Design and development of batch fabricatable metal-insulator-metal diode and microstrio slot antenna as rectenna elements,” Sensors and Actuators A, Vol. 142, pp. 40-47, 2008.

[48] D. Diesing, A. W. Hassel and M. M. Lohrengel, “Aluminium oxide tunnel junctions: influence of preparation technique, sample geometry and oxide thickness,” Thin Solid Films, Vol. 342, pp. 282-290, 1999.

[49] J. F. Shackelford and W. Alexander, CRC Materials Science and Engineering Handbook 3rd ed., CRC, 2000.

[50] S. C. Jones and Y. M. Gupta, “Refractive index and elastic properties of z-cut quartz shocked to 60 kbar,” J. Appl. Phys. Vol. 88, No. 10, pp. 5671-5679, 2000.

[51] K. H. Chen, C. V. Hsu and D. C. Su, “A method for measuring the complex refractive index and thickness of a thin metal film,” J. Appl. Phys. B. Vol. 77, pp. 839-842, 2003.

[52] W. H. Cheng, S. F. Chi and A. K. Chu, “Effect of thermal stresses on temperature dependence of refractive index for Ta_2O_5 dielectric films,” Thin Solid films, Vol. 347, pp. 233-237, 1999.

[53] Y. L. Chiou, J. P. Gambino and M. Mohammad, “Determination of the Fowler-Nordheim tunnelling parameters from the Fowler-Nordheim plot,” Solid State Electronics, Vol. 45, pp. 1787-1791, 2001